

Stability of hexagonal pattern in Rayleigh–Bénard convection for thermodependent shear-thinning fluids

T. Varé¹, C. Nouar^{1,†}, C. Métivier¹ and M. Bouteraa¹

¹LEMETA, UMR 7563 CNRS-Université de Lorraine, 2 Avenue de la Forêt de Haye, TSA 60604, 54518 Vandoeuvre lès Nancy CEDEX, France

(Received 9 January 2020; revised 6 July 2020; accepted 8 September 2020)

Stability of hexagonal patterns in Rayleigh–Bénard convection for shear-thinning fluids with temperature-dependent viscosity is studied in the framework of amplitude equations. The rheological behaviour of the fluid is described by the Carreau model and the relationship between the viscosity and the temperature is of exponential type. Ginzburg–Landau equations including non-variational quadratic spatial terms are derived explicitly from the basic hydrodynamic equations using a multiple scale expansion. The stability of hexagonal patterns towards spatially uniform disturbances (amplitude instabilities) and to long wavelength perturbations (phase instabilities) is analysed for different values of the shear-thinning degree α of the fluid and the ratio r of the viscosities between the top and bottom walls. It is shown that the amplitude stability domain shrinks with increasing shear-thinning effects and increases with increasing the viscosity ratio r . Concerning the phase stability domain which confines the range of stable wavenumbers, it is shown that it is closed for low values of r and becomes open and asymmetric for moderate values of r . With increasing shear-thinning effects, the phase stability domain becomes more decentred towards higher values of the wavenumber. Beyond the stability limits, two different modes go unstable: longitudinal and transverse modes. For the parameters considered here, the longitudinal mode is relevant only in a small region close to the onset. The nonlinear evolution of the transverse phase instability is investigated by numerical integration of amplitude equations. The hexagon–roll transition triggered by the transverse phase instability for sufficiently large reduced Rayleigh number ϵ is illustrated.

Key words: Bénard convection, pattern formation

1. Introduction

Convection of a fluid confined between two parallel horizontal plates and heated from below (Rayleigh–Bénard convection, RBC) is a paradigm of pattern-forming instabilities in spatially extended nonlinear systems (Bodenschatz, Pesch & Ahlers 2000). When the control parameter, i.e. the temperature difference across the fluid layer or the Rayleigh number, exceeds a critical value, the rest state is replaced by motions that organize themselves to form a convective pattern. Increasing further the control parameter, a transition between convective patterns of different symmetries may occur at a

† Email address for correspondence: cherif.nouar@univ-lorraine.fr

second threshold. For modelling processes in geoscience as well as in many industrial systems, the variation of the viscosity with temperature has to be taken into account. A spatially varying viscosity causes additional nonlinear coupling between the temperature and the velocity field and breaks the up–down reflection symmetry with respect to the midplane of the fluid layer. This breaking symmetry modifies the onset of convection and affects the selection of the pattern convection.

1.1. *Effect of temperature-dependent viscosity on the onset of convection*

The effect of a temperature-dependent viscosity on the onset of convection was first studied by Palm (1960) in the case of free–free boundary conditions. Palm (1960) assumed that the kinematic viscosity ν varies as $\nu = \nu_1 + \Delta\nu \cos(b(T - T_1))$, where $\Delta\nu$ is the difference in the viscosity between the top and bottom boundaries, b is a constant and T_1 is the temperature at the bottom of the fluid layer. In his analysis, it is required that $\Delta\nu/\nu_1 \ll 1$. It is found that the critical Rayleigh number Ra_c defined with the average viscosity ν_0 as well as the critical wavenumber k_c decreases with increasing the viscosity variation $\Delta\nu$. They differ by $O(\Delta\nu/\nu_0)^2$ from that obtained with constant viscosity. The decrease of Ra_c and k_c with increasing $\Delta\nu$ was confirmed by Stengel, Olivier & Booker (1982) in free–free and rigid–rigid boundary conditions when a cosine law is used for the dynamic viscosity $\mu(T)$. Busse & Frick (1985) assumed, for numerical convenience, a linear dependence of the viscosity on temperature. The onset of convection is determined in the case of rigid boundary conditions. The variation of Ra_c and k_c as a function of the viscosity ratio $r = \mu_{max}/\mu_{min}$ is quite similar to that obtained by Palm (1960) using cosine law for $\mu(T)$. As pointed out by Busse & Frick (1985), for cosine and linear functions $\mu(T)$, the viscosity at the midplane equals to the average viscosity of the static layer, this is why Ra_c decreases with increasing r . However, if an exponential viscosity variation is used, the average viscosity exceeds the value used in the definition of Ra_c . In this case, the critical Rayleigh number Ra_c increases, reaches a maximum of $Ra_c \approx 2200$ at a viscosity ratio $r \approx 3000$ and then decreases (Stengel *et al.* 1982). This result was confirmed by White (1988). It can be explained by a simple physical argument based on the idea that convection begins first in the sublayer with maximum Rayleigh number. Actually, for a large viscosity contrast, the convection is confined to the sublayer near the hot boundary, and a stagnant zone develops near the cold (top) boundary (Stengel *et al.* 1982; Davaille & Jaupart 1993; Solomatov 1995). Whereas, for cosine and linear laws $\mu(T)$, the convection occurs throughout the entire fluid layer. The onset of two-dimensional convection with strongly temperature-dependent viscosity has been also considered by Bottaro, Metzener & Matalon (1992), assuming Arrhenius law. In this case, the viscosity ratio depends on the temperature difference across the fluid layer and on the temperature level, while for exponential law, the viscosity ratio depends only on the temperature difference. Bottaro *et al.* (1992) found that depending on the reference temperature, the dependence of the critical Rayleigh number Ra_c on the viscosity ratio across the layer may have one of the two behaviours described previously. Either, Ra_c decreases with increasing the viscosity ratio as predicted by Palm (1960) and Busse & Frick (1985), or Ra_c increases initially with increasing the viscosity ratio, reaches a maximum and then decreases as predicted by Stengel *et al.* (1982). Actually, there are two controlling factors that play opposing roles. The reduced thickness of the active layer on one hand requires a larger Rayleigh number for the onset of convection. On the other hand, the fluid layer near the heated wall is less stable because of the decrease of the viscosity.

1.2. Influence of temperature-dependent viscosity on the planform near the onset

In Rayleigh–Bénard convection, under Boussinesq conditions, i.e. when only the temperature variations of the density across the fluid layer are kept, convection in the form of rolls emerge at the onset via a supercritical bifurcation. However, in situations with sufficiently large temperature differences, such that the temperature dependence of the material cannot be neglected, i.e. in non-Oberbeck–Boussines (NOB) convection, the primary bifurcation is transcritical and the nonlinear state that forms beyond it consists of hexagonal cells. The occurrence of a hexagonal pattern can be explained by the triadic wavevector interactions enabled by the quadratic term in the amplitude equations. The temperature dependence is usually the dominant case of asymmetry in convection layers, and its importance for the preference of hexagons was supported theoretically by Palm (1960), Palm, Ellingsen & Gjevik (1967), Segel & Stuart (1962), Busse (1967), Palm (1975) and experimentally by Hoard, Robertson & Acrivos (1970), Somerscales & Dougherty (1970), Stengel *et al.* (1982), Richter (1978), White (1988), Pampaloni *et al.* (1992). Note that for liquids where the viscosity decreases with increasing temperature, the fluid ascends in the central part of the hexagon and descends in the peripheral parts.

According to weakly nonlinear theory, the primary bifurcation to hexagons is associated with a saddle node located at $Ra < Ra_c$. With increasing the heating, a Rayleigh number Ra_r is reached beyond which rolls and hexagons can exist, until Ra_h where hexagons become unstable. This classical NOB scenario was quantified in a pioneering paper of Busse (1967). Actually, at $Ra_r < Ra < Ra_h$, hexagons and rolls are not equally stable, because they are characterized by different values of the specific potential (Lyapunov functional), which depend on the amplitude of rolls sets that constitute the pattern. The transition should occur at Ra_T where the potential is the same for rolls and hexagons. Near Ra_T , the metastable state is replaced by the absolute stable state when a sufficiently strong disturbance is imposed. The range of Ra , where the metastable state coexists with the absolute state defines a region of hysteretic transition (Getling 1988; Pampaloni *et al.* 1992). Some discrepancies exist between theoretical predictions made for an unbounded layer of liquid and experiments in convective cells with a finite aspect ratio (Ciliberto, Pampaloni & Perez-Garcia 1988).

Besides rolls and hexagons, a new planform in the form of squares was observed when the viscosity contrast between upper and lower boundaries exceed a value of order ten (Stengel *et al.* 1982; White 1988). The planform selection problem between rolls and squares was analysed by Busse & Frick (1985) with the assumption that the viscosity varies linearly with temperature. They found that near the critical conditions, rolls are preferred for low values of r , but squares are preferred for large values of r . The change from rolls to squares occurs at $r \approx 2$. Jenkins (1987) used a weakly nonlinear method to investigate the stability of squares. In the case of a linear variation of the viscosity with temperature he found that the transition from rolls to squares occurs at $r \approx 3.2$. The disagreement with Busse & Frick (1985) was not clarified in the literature. For exponential fluids, Jenkins (1987) found that the transition occurs at $r \approx 3$.

1.3. Secondary instabilities

Above onset, there is a range of wavenumbers for which stationary convecting patterns can exist. The existence of these stationary states does not guarantee their physical relevance; they must also themselves be stable to infinitesimal disturbances. A variety of secondary instabilities occur and restrict the domain of stable convection.

In a series of papers, Busse and co-workers Busse (1967), Busse & Whitehead (1971), Clever & Busse (1974) and Busse (1978) gave a complete classification of secondary

instabilities that restrict the region of stable straight convection rolls in Rayleigh–Bénard convection. The region of stable roll convection is often referred to as the ‘Busse balloon’.

The nature of secondary instabilities in more complex patterns such as squares or hexagons is not as well studied as rolls. In the case of a hexagonal pattern it is shown that the secondary instability is induced by long wavelength modulation of the phase of the pattern. In the Bénard–Marangoni problem estimates of the size and shape of a stable band of wavenumbers have been made by Echebarria & Pérez-García (1998) and Young & Riecke (2002) using amplitude equations.

1.4. *Case of non-Newtonian fluids: influence of shear-thinning effects*

Compared to the Newtonian case, very few studies were devoted to non-Newtonian fluids despite their common occurrence in natural systems, food, chemical and petrochemical engineering processes. Most non-Newtonian fluids have two common properties: viscoelasticity and shear-thinning. The influence of the elastic response, in particular the possibility of oscillatory convection due to elastic restoring forces are discussed in the literature; see, for instance, Larson (1992) and the references therein. Compositional effects may also exist as advocated by Kolodner (1998). The pattern selection has been also considered in the literature, e.g. Li & Khayat (2005).

Here, we neglect the elastic response. We focus only on the shear-thinning effects, i.e. the influence of nonlinear decrease of the viscosity with the shear rate. This feature, when it is sufficiently strong, leads to a subcritical bifurcation (Lamsaadi, Naimi & Hasnaoui 2005; Solomatov & Barr 2006, 2007; Balmforth & Rust 2009; Albaalbaki & Khayat 2011; Alloui *et al.* 2013; Benouared, Mamou & Ait-Messaoudene 2014; Bouteraa *et al.* 2015; Jenny, Plaut & Briard 2015). Indeed, in the presence of a finite amplitude perturbation, the viscosity decreases reducing by this way the viscous damping. In the case of RBC in Carreau fluids between two plates of infinite extent maintained at two different temperatures, the shear-thinning degree $\alpha = |d\mu/d\Gamma|_{\Gamma=0}$ above which the bifurcation becomes subcritical has been determined using a weakly nonlinear analysis. The critical value of the shear-thinning degree is $\alpha_c = 24/601\pi^4$ for stress-free boundary conditions (Balmforth & Rust 2009) and $\alpha_c = 2.15 \times 10^{-4}$ for no-slip boundary conditions. In the previous expression, the viscosity μ and the second invariant of the strain rate deformation Γ (defined by (2.7)) are rendered dimensionless using the zero-shear-rate viscosity and thermal diffusion time as characteristic scales. Bouteraa *et al.* (2015) have also studied the stability of the convective patterns near the onset. They show that the only stable patterns are rolls in the supercritical bifurcation. Using two-dimensional nonlinear computations of rolls solutions in Carreau fluids with $\alpha > \alpha_c$, the threshold value of the Rayleigh number has been determined by Benouared *et al.* (2014) and Jenny *et al.* (2015) for a large range of rheological parameters.

Very few experimental studies dealing with RBC in shear-thinning fluids exist in the literature. Liang & Acrivos (1970) were the first to study experimentally the onset of convection in horizontal layers of dilute aqueous solutions of polyacrylamide. These fluids are shear-thinning with approximately constant viscosity at low shear rates. The shear-thinning degree α is less than α_c . The experimental set-up consists of a rectangular cavity with the length to height aspect ratio $AR \approx 25$. Liang & Acrivos (1970) found that the critical Rayleigh number is practically the same as for a Newtonian fluid. The flow patterns detected by visualizations using aluminium flakes as tracers, consist of two-dimensional rolls with a transition to a three-dimensional structure at much higher Rayleigh number. To our knowledge, since Liang & Acrivos in the 1970s, there is no more

experimental data until 2016. Darbouli *et al.* (2016) investigated experimentally the RBC in shear-thinning fluids in a cylindrical cell using a magnetic resonance imaging (MRI) technique. The aspect ratio of the cylindrical cavity, i.e. diameter-to-height ratio is $AR = 6$. Actually, the aspect ratio value is imposed by the diameter of the MRI resonator (Darbouli *et al.* 2016). The fluids used are xanthan gum solutions at different concentrations, which rheological behaviour can be described by the Carreau model. In these experiments, $\alpha < \alpha_c$. For a concentration of 1000 ppm, the patterns observed above the criticality consist of patches of fairly regular rolls linked by lines of disclinations. With increasing the concentration of xanthan gum, the shear-thinning effects as well as the viscosity plateau at low shear rates increase. A larger temperature difference is therefore needed for the onset of convection. The non-Oberbeck–Boussinesq effects become significant and convection in the form of ‘polygons’ occurs at the onset. With increasing Ra , a transition to rolls is observed. This study was supplemented by Bouteraa (2016) using a shadowgraph method for pattern visualization. The experimental set-up is identical to that in Darbouli *et al.* (2016). For a sufficiently high concentration of xanthan gum, hexagonal patterns are clearly observed at the onset, followed by a range of Rayleigh numbers where the two solutions rolls and hexagons coexist with topological defects. A deeper analysis indicates that the wavenumber of the hexagonal pattern increases with Ra .

In another context, RBC in shear-thinning fluids with strong variation of the viscosity with temperature has been studied numerically in two-dimensional layers by Solomatov & Barr (2007), Solomatov & Barr (2007) and Kaddiri *et al.* (2012). The viscosity ratio r between the top and bottom walls is greater than 10^3 . In this case, the convection takes place in the so-called stagnant-lid regime. The objective was to understand the convection in the interiors of the Earth and other planets whose viscosity is a much stronger function of temperature. In these studies, the power-law model is adopted for the rheological behaviour. The primary bifurcation is subcritical and it is shown that the threshold value of the Rayleigh number Ra_1 for the onset of convection decreases with increasing shear-thinning effects and viscosity contrasts. A correlation relating Ra_1 to the shear-thinning index and the viscosity ratio is proposed.

To summarize:

- (a) In the frame of Boussinesq approximations, theoretical studies show that for sufficiently strong shear-thinning effects, the primary bifurcation becomes subcritical. In this case, the threshold values of the Rayleigh number for the onset of convection have been determined from numerical computations in two-dimensional layers.
- (b) In the frame of Boussinesq approximations, and in the supercritical regime, theoretical studies show that near the onset, only rolls are stable and shear-thinning effects reinforce convection in the form of rolls.
- (c) Recent experimental investigations of Rayleigh–Bénard convection in shear-thinning polymer solutions show that steady hexagonal patterns with upflow at the centre arise at the onset, because of NOB effects, followed by a range in Ra , where rolls and hexagons coexist. Furthermore, for the hexagonal pattern, the wavenumber selected by the system increases with increasing Ra .

1.5. Objectives, methodology and outline of the paper

It is clear that the theoretical predictions of Rayleigh–Bénard convection in shear-thinning fluids done within the framework of Boussinesq approximations cannot be used to describe at least qualitatively the experimental results.

The objective of the present work is to investigate the influence of shear-thinning effects and the variation of the viscosity with temperature on the pattern selection, its stability and the range of stable wavenumbers. The rheological law introduces an additional nonlinear coupling between the flow variables. A weakly nonlinear analysis is used as a first approach to study nonlinear effects. Amplitude equations are derived and the instabilities of hexagonal patterns with respect to homogeneous and longwave perturbations are calculated.

The present work considers a laterally infinite system. Therefore, it is difficult to have a direct correspondance with the experimental results obtained with an apparatus of a small aspect ratio such as that used by Darbouli *et al.* (2016) and Bouteraa (2016). Indeed, the finite size and the no-slip boundary conditions at the lateral walls affect the Rayleigh number at the convective threshold (Charlson & Sani 1970) and introduces topological defects such as dislocations and disclinations which play a significant role in the roll–hexagon competition (Ciliberto *et al.* 1990) as well as on the mechanism of wavenumber selection (Pocheau & Croquette 1984). Nonetheless, we expect a qualitative comparison.

Note that for moderate values of the viscosity ratio r , a competition between rolls and hexagons is concerned. When the viscosity ratio exceeds a limit value r_ℓ , rolls become unstable to squares. Except in the linear stability analysis where a large range of r is considered, in the rest of the paper we consider only the case where $1 < r \leq r_\ell$ as in Darbouli *et al.* (2016) and Bouteraa (2016).

This paper is organized as follows. We start with the governing equations in § 2. The linear stability analysis is presented in § 3. The weakly nonlinear analysis using a multiple scale method is presented in § 4. The amplitude equations for hexagons are derived and the different coefficients are determined as a function of shear-thinning effects and the viscosities ratio. In § 5 the limit value of the viscosity ratio above which rolls become unstable to squares is determined as a function of shear-thinning effects. The relative stability of homogeneous hexagons and rolls is discussed in § 6. Then, in § 7 the stability of hexagons with respect to long wavelength perturbations is addressed. The phase equations are derived and the range of stable wavenumbers is determined. Numerical simulations of the amplitude equations are presented in § 8. The nonlinear evolution of the instabilities and the formation of defects are investigated. Finally, a brief summary of the results is given in § 9.

2. Basic equations

Hereafter, quantities with hats are dimensional quantities. We consider a layer of shear-thinning fluid of depth \hat{d} confined between two impermeable horizontal plates, infinite in extent, which are perfect heat conductors. The bottom and top plates are kept at constant temperatures, respectively, $\hat{T}_0 + \delta\hat{T}/2$ and $\hat{T}_0 - \delta\hat{T}/2$, with $\delta\hat{T} > 0$. The fluid has density $\hat{\rho}$, thermal diffusivity $\hat{\kappa}$, thermal expansion coefficient $\hat{\beta}$ and viscosity $\hat{\mu}_0$ at zero shear rate. In the absence of convection the heat conducting state is described by

$$\hat{\mathbf{u}} = \mathbf{0}, \quad \frac{d\hat{P}}{d\hat{z}} = -\hat{\rho}_0\hat{g}[1 - \hat{\beta}(\hat{T}_{cond} - \hat{T}_0)], \quad \hat{T}_{cond} - \hat{T}_0 = \frac{\delta\hat{T}}{2} \left(1 - \frac{2\hat{z}}{\hat{d}}\right), \quad (2.1a-c)$$

where $\hat{\mathbf{u}}$ is the fluid velocity, \hat{P} is the pressure and \hat{T}_0 is the mean of the boundary temperatures. The z -axis is directed upwards, with its origin located at the bottom plate. The stability of the hydrostatic solution is considered by introducing temperature and

pressure perturbations as well as a fluid motion. Using the units $\hat{d}^2/\hat{\kappa}$, \hat{d} , $\hat{\kappa}/\hat{d}$ and $\delta\hat{T}$ for time, length, velocity and temperature, the dimensionless perturbation equations are

$$\nabla \cdot \mathbf{u} = 0, \tag{2.2}$$

$$\frac{1}{Pr} \left[\frac{\partial \mathbf{u}}{\partial t} + (\mathbf{u} \cdot \nabla) \mathbf{u} \right] = -\nabla p + Ra \theta \mathbf{e}_z + \nabla \cdot \boldsymbol{\tau}, \tag{2.3}$$

$$\frac{\partial \theta}{\partial t} + \mathbf{u} \cdot \nabla \theta = \mathbf{u} \cdot \mathbf{e}_z + \nabla^2 \theta. \tag{2.4}$$

Here, \mathbf{e}_z denotes the unit vector in the vertical direction, $p(\mathbf{x}, t)$ and $\theta(\mathbf{x}, t)$ represent the pressure and temperature deviations from their values in the conductive state. The Boussinesq approximations are taken into account, i.e. the variation of the density is neglected except in the buoyancy term. Denote by (x, y, z) the components of the position vector \mathbf{x} , and (u, v, w) the components of the velocity vector \mathbf{u} . The Rayleigh number Ra and the Prandtl number Pr are

$$Ra = \frac{\hat{\rho}_0 \hat{g} \hat{\beta} \delta \hat{T} \hat{d}^3}{\hat{\kappa} \hat{\mu}_0}; \quad Pr = \frac{\hat{\mu}_0}{\hat{\rho}_0 \hat{\kappa}}. \tag{2.5a,b}$$

The reference viscosity, $\hat{\mu}_0$, is the zero-shear-rate viscosity evaluated at \hat{T}_0 , i.e. the mean of the boundary temperatures.

2.1. Rheological model and parameters

The fluid is assumed to be purely viscous and shear-thinning. The viscous stress tensor

$$\boldsymbol{\tau} = \mu(\Gamma) \dot{\boldsymbol{\gamma}} \quad \text{with} \quad \dot{\boldsymbol{\gamma}} = \nabla \mathbf{u} + (\nabla \mathbf{u})^T \tag{2.6}$$

the rate-of-strain tensor, of second invariant

$$\Gamma = \frac{1}{2} \dot{\gamma}_{ij} \dot{\gamma}_{ij}. \tag{2.7}$$

We assume a Carreau-law fluid where the viscosity depends exponentially on temperature,

$$\frac{\mu - \mu_\infty}{\mu_0 - \mu_\infty} = \exp[-\hat{b}(\hat{T} - \hat{T}_0)] \left(1 + \hat{\lambda}^2 \hat{\Gamma} \right)^{(n_c - 1)/2}, \tag{2.8}$$

with $\mu_0 = \hat{\mu}_0/\hat{\mu}_0$ and $\mu_\infty = \hat{\mu}_\infty/\hat{\mu}_0$ are the viscosities at low and high shear rate, \hat{b} is the thermodependency coefficient which measures the sensitivity of viscosity to variation in temperature, $n_c < 1$ is the shear-thinning index and $\hat{\lambda}$ is the characteristic time of the fluid. The characteristic shear rate for the onset of shear-thinning is determined by $1/\hat{\lambda}$. The infinite shear viscosity, $\hat{\mu}_\infty$, is generally significantly smaller (10^3 to 10^4 times smaller) than $\hat{\mu}_0$ (Bird, Armstrong & Hassager 1987; Tanner 2000). The ratio $\hat{\mu}_\infty/\hat{\mu}_0$ will be thus neglected in the following. The exponential model used for the viscosity thermodependency is referred to in the literature as the Frank–Kamenetski model and can be derived from the Arrhenius law by expanding the arguments of the exponential (in the Arrhenius law) in a Taylor series about the reference temperature \hat{T}_0 (Bottaro *et al.* 1992).

The dimensionless effective viscosity is then

$$\mu = \frac{\hat{\mu}}{\hat{\mu}_0} = \mu_b(z) \exp(-c\theta)(1 + \lambda^2 \Gamma)^{(n_c-1)/2}, \tag{2.9}$$

where $\mu_b(z) = \exp(c(z - 1/2))$ is the viscosity profile at quiescent state, $c = \hat{b}\delta\hat{T}$ is a measure of the viscosity contrast and $\lambda = \hat{\lambda}/(\hat{d}^2/\hat{\kappa})$ is a dimensionless characteristic time of the fluid. The Newtonian behaviour, $\hat{\mu} = \hat{\mu}_0$, is obtained by setting $n_c = 1$ or $\hat{\lambda} = 0$. The viscosity ratio across the fluid layer,

$$r = \frac{\mu_b(z = 1)}{\mu_b(z = 0)} \quad \text{with } \ln(r) = c = \hat{b}\delta\hat{T}, \tag{2.10}$$

depends on \hat{b} and $\delta\hat{T}$, but not on the temperature level. For a small amplitude disturbance, the viscosity can be expanded about the hydrostatic solution,

$$\mu = \mu_b [1 - c\theta + \dots] \left[1 + \left(\frac{n_c - 1}{2} \right) \lambda^2 \Gamma + \dots \right]. \tag{2.11}$$

At the second-order Taylor expansion of $(1 + \lambda^2 \Gamma)^{(n_c-1)/2}$, a relevant rheological parameter, i.e. the ‘degree of shear-thinning’ appears:

$$\alpha = \left. \frac{d\mu}{d\Gamma} \right|_{\Gamma=0} = \frac{1 - n_c}{2} \lambda^2. \tag{2.12}$$

2.2. Boundary conditions

For the velocity field, no-slip boundary conditions are considered. For the temperature deviation, the thermal conductivity of the boundaries is assumed much larger than that of the fluid, so that their temperature remains ‘fixed’. The boundary conditions are then

$$\theta = u = v = w = 0 \quad \text{on } z = 0, 1. \tag{2.13}$$

2.3. Reduction: elimination of the pressure

Applying twice the curl to momentum equations (2.3) and using the continuity equation, we get the following evolution equations for the velocity components w , u and v :

$$\begin{aligned} \frac{1}{Pr} \frac{\partial}{\partial t} \Delta w &= \frac{1}{Pr} \left[\frac{\partial^2}{\partial y \partial z} \mathcal{N}(v) + \frac{\partial^2}{\partial x \partial z} \mathcal{N}(u) - \Delta_H \mathcal{N}(w) \right] + Ra \Delta_H \theta \\ &+ \mu_b \Delta^2 w + 2 \left(\frac{d\mu_b}{dz} \right) \Delta \left(\frac{\partial w}{\partial z} \right) + \frac{d^2 \mu_b}{dz^2} \left(\frac{\partial^2 w}{\partial z^2} - \Delta_H w \right) \\ &+ \left[\Delta_H \mathcal{N} V_z - \frac{\partial^2}{\partial x \partial z} \mathcal{N} V_x - \frac{\partial^2}{\partial y \partial z} \mathcal{N} V_y \right], \end{aligned} \tag{2.14}$$

$$\begin{aligned} \frac{1}{Pr} \frac{\partial}{\partial t} \left[\Delta_H u + \frac{\partial^2 w}{\partial x \partial z} \right] &= \frac{1}{Pr} \left[\frac{\partial^2}{\partial x \partial y} \mathcal{N}(v) - \frac{\partial^2}{\partial y^2} \mathcal{N}(u) \right] + \mu_b \Delta \left[\Delta_H u + \frac{\partial^2 w}{\partial x \partial z} \right] \\ &+ \frac{d\mu_b}{dz} \frac{\partial}{\partial z} \left[\Delta_H u + \frac{\partial^2 w}{\partial x \partial z} \right] - \frac{\partial}{\partial y} \mathcal{N} V_z, \end{aligned} \tag{2.15}$$

$$\begin{aligned} \frac{1}{Pr} \frac{\partial}{\partial t} \left[\Delta_H v + \frac{\partial^2 w}{\partial y \partial z} \right] &= \frac{1}{Pr} \left[\frac{\partial^2}{\partial x \partial y} \mathcal{N}(u) - \frac{\partial^2}{\partial x^2} \mathcal{N}(v) \right] + \mu_b \Delta \left[\Delta_H v + \frac{\partial^2 w}{\partial y \partial z} \right] \\ &+ \frac{d\mu_b}{dz} \frac{\partial}{\partial z} \left[\Delta_H v + \frac{\partial^2 w}{\partial y \partial z} \right] + \frac{\partial}{\partial x} \mathcal{N}V_z. \end{aligned} \tag{2.16}$$

Here the ‘horizontal Laplacian’ is defined by

$$\Delta_H = \frac{\partial^2}{\partial x^2} + \frac{\partial^2}{\partial y^2}. \tag{2.17}$$

The nonlinear inertial terms $\mathcal{N}(\cdot)$ and nonlinear viscous terms $\mathcal{N}V_x$ are defined by

$$\mathcal{N}(\cdot) = (\mathbf{u} \cdot \nabla)(\cdot); \quad \mathcal{N}V_x = [\nabla \cdot ((\mu - \mu_b)\dot{\boldsymbol{\gamma}})] \cdot \mathbf{e}_x, \tag{2.18a,b}$$

similarly for $\mathcal{N}V_y$ and $\mathcal{N}V_z$. The boundary conditions are

$$\theta = w = \frac{\partial w}{\partial z} = u = v = 0 \quad \text{at } z = 0, 1. \tag{2.19}$$

In a matrix notation, the system (2.14)–(2.16), (2.4) can be written formally as

$$M \frac{\partial \boldsymbol{\Psi}}{\partial t} = L\boldsymbol{\Psi} + NI + NV, \tag{2.20}$$

where $\boldsymbol{\Psi} = (w, u, v, \theta)^t$, the operators M, L, NI and NV represent the weight matrix, the linear operator, the nonlinear inertial operator and the nonlinear viscous operator, respectively. The nonlinear operators can also be decomposed as

$$NI = [NI_w, NI_u, NI_v, NI_\theta]^t \quad \text{and} \quad NV = [NV_w, NV_u, NV_v, 0]^t. \tag{2.21a,b}$$

3. Linear stability analysis

In linear theory $\mathbf{u}(u, v, w)$ and θ are assumed infinitesimal and the nonlinear terms in (2.14)–(2.16) and (2.4) are neglected. As the horizontal extent is taken infinite, the disturbance quantities w, u, v, θ are assumed periodic and of the form

$$(w, u, v, \theta) = (F_{11}(z), U_{11}(z), V_{11}(z), G_{11}(z))f(x, y) \exp(st), \tag{3.1}$$

with $f(x, y) = \exp(ik_x x + ik_y y)$, $\mathbf{k} = (k_x, k_y, 0)$ the horizontal wavenumber and $s = s_r + is_i$ a complex number. This leads to the eigenvalue problem

$$\begin{aligned} sPr^{-1}(D^2 - k^2)F_{11} &= \mu_b(D^2 - k^2)^2 F_{11} + 2D\mu_b(D^2 - k^2)DF_{11} \\ &+ D^2\mu_b(D^2 + k^2)F_{11} - k^2 RaG_{11}, \end{aligned} \tag{3.2}$$

$$sG_{11} = F_{11} + (D^2 - k^2)G_{11}, \tag{3.3}$$

with D the derivative with respect to z and k the norm of the vector \mathbf{k} . Note that at this order, no non-Newtonian effects enter the problem and the thermodependency appears

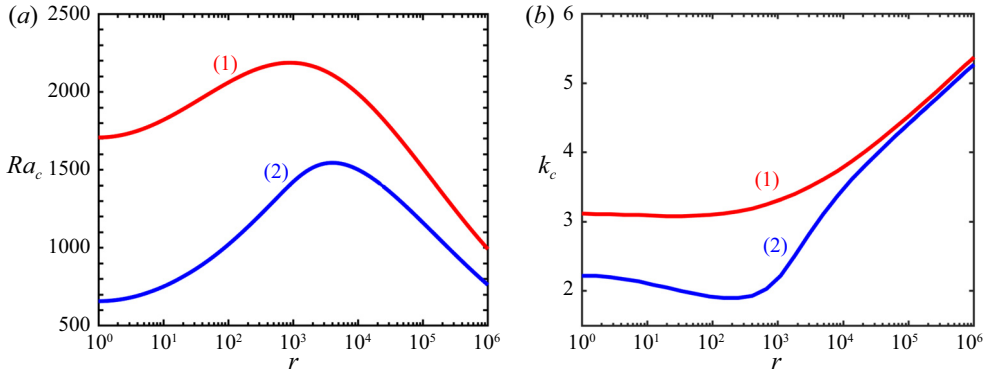


FIGURE 1. Exponential fluid. Critical Rayleigh number (a) and critical wavenumber (b) as a function of the viscosity ratio. (1) NSBC, (2) SFBC.

through the viscosity profile of the base state $\mu_b(z)$. The boundary conditions are

$$F_{11} = DF_{11} = G_{11} = 0 \quad \text{at } z = 0, 1. \tag{3.4}$$

The eigenvalue problem (3.2) and (3.3) where s is the eigenvalue and $X_{11} = (F_{11}, G_{11})$ the eigenvector can be written formally as

$$s\tilde{M} \cdot X_{11} = \tilde{L} \cdot X_{11}. \tag{3.5}$$

It is easy to show that the principle of exchange of stability still holds, i.e. $s_i = 0$, when the viscosity profile is not uniform. Since any multiple of the eigenvector X_{11} is also a solution of (3.5), X_{11} has to be normalized. We have adopted the same normalization as in Bouteraa *et al.* (2015):

$$G_{11}(z = 1/2) = 1. \tag{3.6}$$

A spectral Chebyshev method is used to determine the critical Rayleigh number and the critical wavenumber (Bouteraa *et al.* 2015). The marginal stability curve $Ra(k)$ is obtained by the condition $s(Ra, k) = 0$. Using 20 Chebyshev polynomials, the first eigenvalue, i.e. that for which the real part is the largest, is calculated with an accuracy of 10^{-4} . The minimum of the marginal stability curves gives the critical Rayleigh number Ra_c and critical wavenumber k_c . In the case of exponential fluids, figure 1 displays the variation of the critical Rayleigh number for the onset of convection, Ra_c , as well as the critical wavenumber, k_c , as a function of the viscosity ratio r for no-slip boundary conditions (NSBC) and stress-free boundary conditions (SFBC). This later was added only as a validation test. Our results are in very good quantitative agreement with those obtained by Stengel *et al.* (1982). As indicated by these authors, three different ranges of the viscosity ratio can be distinguished. (i) At low viscosity ratio, $0 \leq r \leq 1.5$, Ra_c and k_c are almost constant. (ii) At moderate viscosity ratio, $1.5 \leq r \leq 8$, Ra_c increases with increasing r and k_c is nearly constant or decreases slightly for SFBC. The viscosity variation in the moderate viscosity ratio stabilizes the conductive state. (iii) For a large viscosity ratio, Ra_c decreases with increasing r and k_c increases rapidly. In this regime, the convection is governed by a sublayer that is more unstable than the full layer (Stengel *et al.* 1982).

As another validation of the linear stability analysis, we have also reproduced the results obtained by Busse & Frick (1985) assuming a linear dependency of the viscosity with temperature.

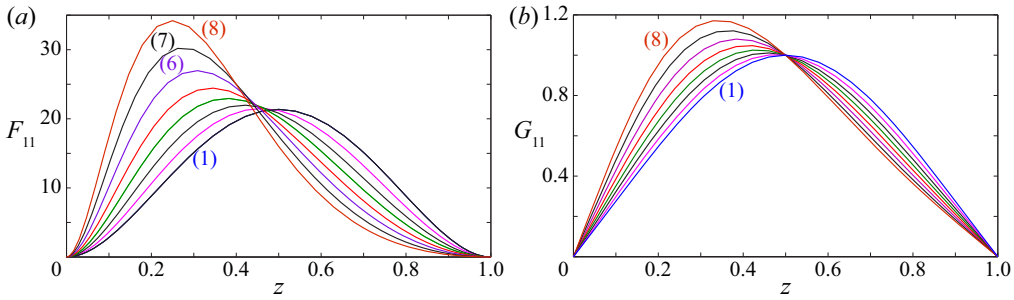


FIGURE 2. Exponential fluid. (a) Vertical velocity eigenfunction and (b) temperature perturbation at the first order as a function of the depth z for different values of the thermodependency coefficient c . (1) $c = 0$; (2) $c = 1$; (3) $c = 2$; (4) $c = 3 \dots$ increasing c by step 1 until curve (8) $c = 7$.

Figure 2 displays, for an exponential fluid, the profiles of the vertical velocity eigenfunction and the temperature perturbation at the first order for different values of the thermodependency coefficient. With increasing the viscosity contrast c , the maximum of $F_{11}(z)$ takes place near the bottom plate where the fluid is less viscous, i.e. the centre of the convection rolls is shifted towards the bottom plate, and the fluid motion is significantly reduced near the top wall. The shear rate increases near the lower boundary and decreases near the upper. The viscosity contrast between the top and lower boundaries could be reinforced by the shear-thinning effects. Similarly, the temperature perturbation becomes more confined near the heated wall. Of course, when $c = 0$, the eigenfunctions, $F_{11}(z)$ and $G_{11}(z)$, are symmetric with respect to the midplane of the fluid layer.

4. Amplitude equations in a hexagonal lattice

The critical Rayleigh number for the onset of convection determined from the linear stability analysis depends only on the norm k_c of the wavevector. Because of the isotropy of the extended horizontal plane, the direction of the wavevector is arbitrary. In addition, any linear combination of modes $A_p \exp(i\mathbf{k}_p \cdot \mathbf{r})(F_{11}(z), G_{11}(z))$, where $\mathbf{r} = (x, y)$, $\mathbf{k}_p = (k_{px}, k_{py})$, $|\mathbf{k}_p| = k_c$ and A_p are constant coefficients is a solution of the linear problem, i.e. there is also a pattern degeneracy. We consider the case where the wavevectors lie on a hexagonal lattice

$$(w, \theta) = \sum_{p=1}^3 A_p (F_{11}, G_{11}) \exp(i\mathbf{k}_p \cdot \mathbf{r}) + \text{c.c.} + \text{h.o.t.}, \tag{4.1}$$

where, ‘c.c.’ denotes the complex conjugate of the prior expression and ‘h.o.t.’ means ‘higher order terms’. The hexagon patterns (see figure 3) are made of three pairs of wavevectors at $2\pi/3$ angles apart: $\mathbf{k}_1 = k_c \mathbf{e}_x$, $\mathbf{k}_2 = k_c(-\mathbf{e}_x/2 + (\sqrt{3}/2)\mathbf{e}_y)$ and $\mathbf{k}_3 = k_c(-\mathbf{e}_x/2 - (\sqrt{3}/2)\mathbf{e}_y)$. The objective is to determine the spatio-temporal evolution of the amplitude A_p , above threshold, due to different nonlinearities of the problem.

4.1. Multiple scales method

As the Rayleigh number is increased above the onset Ra_c , the growth rate of the perturbation is positive for any wavenumber within a band $\sqrt{\epsilon}$ around the critical

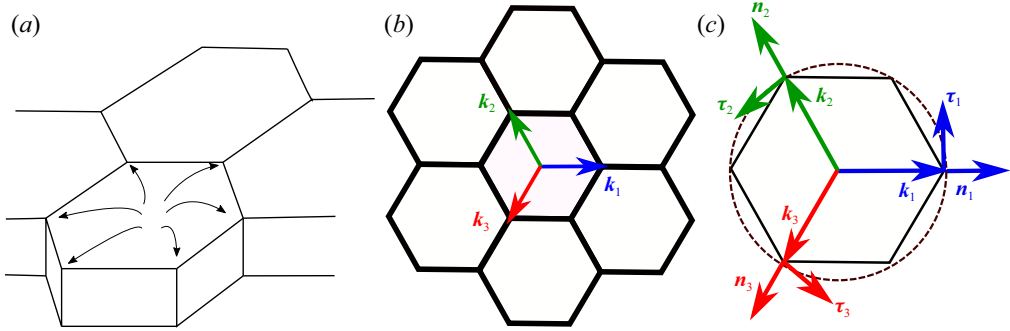


FIGURE 3. (a) Hexagonal convection with flow up in the centre. (b) Basic wavevectors of hexagonal pattern. (c) Unit vectors: n_i parallel and τ_i perpendicular to the wavevector.

wavenumber, where $\epsilon = (Ra - Ra_c)/Ra_c$ is the distance from the onset. Indeed, Taylor expansion of the dispersion curve near its maximum shows that $s \propto \epsilon$ and $(k - k_c) \propto \sqrt{\epsilon}$. For $\epsilon > 0$, emergent patterns are described by an infinite sum of unstable modes (in a continuous band) of the form $\exp(\epsilon t/\tau_0) \exp(ik_c x) \exp(i(\sqrt{\epsilon}x/\xi_0))$. Here, τ_0 is the characteristic time for the instability to grow and ξ_0 is the coherence length. For small ϵ , we can separate the dynamics into fast eigenmodes and slow modulation of the form $\exp(\epsilon t/\tau_0) \exp(i(\sqrt{\epsilon}x/\xi_0))$. A similar reasoning can be done for the y -direction.

Let us denote $\delta = \sqrt{\epsilon}$. The multiple scales approach is used to obtain the amplitude equation, which describes the slow temporal and spatial variation of the variables. The slow scales

$$X = \delta x, \quad Y = \delta y \quad \text{and} \quad T = \delta^2 t \tag{4.2a-c}$$

are treated as independent of the fast scales x, y and t . The derivatives with respect to the new variables are

$$\frac{\partial}{\partial t} \longrightarrow \frac{\partial}{\partial t} + \delta^2 \frac{\partial}{\partial T}, \quad \frac{\partial}{\partial x} \longrightarrow \frac{\partial}{\partial x} + \delta \frac{\partial}{\partial X}, \quad \frac{\partial}{\partial y} \longrightarrow \frac{\partial}{\partial y} + \delta \frac{\partial}{\partial Y}, \quad \frac{\partial}{\partial z} \longrightarrow \frac{\partial}{\partial z}. \tag{4.3a-d}$$

The fast spatial variables vary on the order of a typical wavelength. The slow variables describe the temporal and the spatial modulations of these fast variables. Furthermore, as the marginal mode is stationary, then

$$\frac{\partial}{\partial t} \longrightarrow \delta^2 \frac{\partial}{\partial T}. \tag{4.4}$$

The solution of the nonlinear problem in the neighbourhood of the critical conditions, corresponding to the onset of convection is developed with respect to the parameter δ by

$$\Psi = \delta \Psi^{(1)} + \delta^2 \Psi^{(2)} + \delta^3 \Psi^{(3)} + O(\delta^4), \tag{4.5}$$

$$Ra = Ra_c + \delta Ra^{(1)} + \delta^2 Ra^{(2)} + O(\delta^3). \tag{4.6}$$

The Taylor expansion is also applied to the operators

$$M = M^{(0)} + \delta M^{(1)} + O(\delta^2), \tag{4.7}$$

$$L = L^{(0)} + \delta L^{(1)} + \delta^2 L^{(2)} + O(\delta^3), \tag{4.8}$$

$$NI = \delta^2 NI^{(2)} + \delta^3 NI^{(3)} + O(\delta^4), \tag{4.9}$$

$$NV = \delta^2 NV^{(2)} + \delta^3 NV^{(3)} + O(\delta^4). \tag{4.10}$$

The explicit expressions of M , L , NI and their sub-scales are given in [appendix A](#). The expressions of NV and its sub-scales are too lengthy, and, thus, are not shown.

4.2. Derivation of the Ginzburg–Landau equation

Taking (4.3a–d) and (4.4) into account, the expansion of variables (4.5), (4.6) and operators (4.7)–(4.10) are substituted formally into the nonlinear system of (2.4), (2.14)–(2.16). After ordering according to the power of δ , a sequence of systems of equations is obtained. In the following, the first three orders are determined.

4.2.1. Solution at order δ

At the first order of δ , the following linearized problem is obtained:

$$L^{(0)}\Psi^{(1)} = 0. \tag{4.11}$$

The system (4.11) corresponds to the linear problem discussed in § 3. However, now $\Psi^{(1)}$ is also a function of the slow variables X , Y and T . These variables do not appear in the linear stability analysis section. For hexagon patterns, the first-order solution $\Psi^{(1)} = [w^{(1)}, u^{(1)}, v^{(1)}, \theta^{(1)}]^t$ is

$$w^{(1)} = F_{11}(z)[A_1 \exp(i\mathbf{k}_1 \cdot \mathbf{r}) + A_2 \exp(i\mathbf{k}_2 \cdot \mathbf{r}) + A_3 \exp(i\mathbf{k}_3 \cdot \mathbf{r})] + \text{c.c.}, \tag{4.12}$$

$$\theta^{(1)} = G_{11}(z)[A_1 \exp(i\mathbf{k}_1 \cdot \mathbf{r}) + A_2 \exp(i\mathbf{k}_2 \cdot \mathbf{r}) + A_3 \exp(i\mathbf{k}_3 \cdot \mathbf{r})] + \text{c.c.}, \tag{4.13}$$

$$\mathbf{u}_H^{(1)} = \frac{DF_{11}}{k^2} \nabla_{Hx} [A_1 \exp(i\mathbf{k}_1 \cdot \mathbf{r}) + A_2 \exp(i\mathbf{k}_2 \cdot \mathbf{r}) + A_3 \exp(i\mathbf{k}_3 \cdot \mathbf{r})] + \text{c.c.}, \tag{4.14}$$

where ∇_{Hx} denotes the horizontal gradient for the fast variables, $\mathbf{u}_H = (u, v)$ the horizontal velocity components and A_p the amplitude of the perturbation

$$A_p = A_p(X, Y, T), \quad p = 1, 2, 3. \tag{4.15}$$

4.2.2. Solution at order δ^2

At the next order δ^2 , we have

$$L^{(0)}\Psi^{(2)} = -L^{(1)}\Psi^{(1)} - NI^{(2)} - NV^{(2)}. \tag{4.16}$$

The forcing terms on the right-hand side of (4.16) are computed by introducing the first-order solution (4.12)–(4.14). It is worthy to note that at the second order, the nonlinear viscous term $[NV]^{(2)}$ is proportional to $c = \ln(r)$. Indeed $[\nabla \cdot (\mu - \mu_b)\dot{\gamma}]$ reduces at the second order to $[-c\nabla \cdot (\mu_b\theta\dot{\gamma})]$. The forcing terms on the right-hand side of (4.16) can be separated in four parts.

- (a) Terms proportional to $|A_p|^2$ ($p = 1, 2, 3$), with the wavenumber modulus $|k| = 0$, due to the interaction of the eigenmode with its complex conjugate.
- (b) Terms proportional to $A_p^2 \exp(2i\mathbf{k}_p \cdot \mathbf{r})$, $|k| = 2k_c$, due to the interaction of the eigenmode with itself.

- (c) Terms proportional to $A_p A_q^* \exp(i(\mathbf{k}_p - \mathbf{k}_q) \cdot \mathbf{r})$, $|\mathbf{k}| = \sqrt{3}k_c$.
 (d) Resonant forcing with wavevector \mathbf{k}_ℓ ($\ell = 1, 2, 3$ and $|\mathbf{k}_\ell| = k_c$).

Four separate sets of non-homogeneous differential equations are then derived for each component. They are given in [appendix B](#). For the fourth component, the right-hand side of the non-homogeneous differential contains secular terms. A solvability condition, known as the Fredholm alternative, should then be applied for a solution to exist, i.e. the left-hand side of (4.16) has to be orthogonal to the null space of the adjoint operator given in [appendix C](#). We obtain

$$\begin{aligned}
 & A_2^* A_3^* \int_0^1 G_{ad}(2F_{11} D G_{11} + G_{11} D F_{11}) dz + A_2^* A_3^* \frac{1}{Pr} \int_0^1 F_{ad}(2D F_{11} D^2 F_{11} + F_{11} D^3 F_{11} \\
 & - 3k_c^2 F_{11} D F_{11} dz) - A_2^* A_3^* \int_0^1 F_{ad} [N V_w]_{A_2^* A_3^*}^{(2)} dz - 2i(\mathbf{k}_1 \cdot \nabla_{HX}) A_1 \\
 & \times \left[2 \int_0^1 \mu_b (D^2 F_{11} - k_c^2 F_{11}) F_{ad} dz + 2 \int_0^1 \frac{d\mu_b}{dz} \frac{dF_{11}}{dz} F_{ad} dz \right] - 2i(\mathbf{k}_1 \cdot \nabla_{HX}) \\
 & \times A_1 \left[- \int_0^1 \frac{d^2 \mu_b}{dz^2} F_{11} F_{ad} dz + Ra_c \int_0^1 G_{11} F_{ad} dz \right] - k_c^2 Ra^{(1)} A_1 \int_0^1 G_{11} F_{ad} dz = 0.
 \end{aligned} \tag{4.17}$$

Two other similar relations are obtained by circular permutation of the indices. In the above equations ∇_{HX} denotes the horizontal gradient for the slow variables. The integrals in (4.17) are evaluated numerically by means of the Clenshaw and Curtis method. The calculation leads to a result of the form

$$Ra^{(1)} A_1 + b A_2^* A_3^* = 0. \tag{4.18}$$

Again, two other similar relations are obtained by circular permutation. These expressions allow us to determine the solution at the second order, $\Psi^{(2)} = [w^{(2)}, u^{(2)}, v^{(2)}, \theta^{(2)}]^t$ which can be written as the sum of four terms. The influence of nonlinear viscous terms proportional to $c = \ln(r)$ is clearly highlighted.

The first term $\Psi_1^{(2)}$ proportional to $|A_p|^2$ correspond to the modification of the base state. It is shown that $u_1^{(2)} = 0$, i.e. there is no velocity for the zero mode. The correction at the second order of the conductive temperature profile $\theta_1^{(2)} = T_1(z)[|A_1|^2 + |A_2|^2 + |A_3|^2]$ is displayed in [figure 4](#). The warm upflow and cold downflow fluid tend to reduce the vertical temperature gradient. This effect is more significant with increasing viscosity ratio.

The second term $\Psi_2^{(2)}$ proportional to $A_p^2 \exp(2i\mathbf{k}_p \cdot \mathbf{r})$ is the first harmonic of the fundamental. Hence, we have $[w_2^{(2)}, \theta_2^{(2)}] = [W_2(z), T_2(z)][A_1^2 E_1^2 + A_2^2 E_2^2 + A_3^2 E_3^2]$, with $E_p = \exp(i\mathbf{k}_p \cdot \mathbf{r})$. The influence of the viscosity ratio r on the profile $W_2(z)$ and $T_2(z)$ is shown in [figure 5](#).

The third term $\Psi_3^{(2)}$ proportional to $A_p A_q^* E_p E_q^*$ results from the quadratic interaction between modes with wavevector \mathbf{k}_p and $(-\mathbf{k}_q)$ with $p \neq q$. We have $[w_3^{(2)}, \theta_3^{(2)}] = [W_3(z), T_3(z)][A_1 A_2^* E_1 E_2^* + A_1 A_3^* E_1 E_3^* + A_2 A_3^* E_2 E_3^*]$. The variations of W_3 and T_3 are displayed in [figure 6](#). The amplitude of these modes increases with r and are more important than that of the first harmonic. The fourth term (resonant term) proportional to $\exp(i\mathbf{k}_p \cdot \mathbf{r})$ is given by $(w_4^{(2)}, \theta_4^{(2)}) = (W_4, T_4)(E_1 + E_2 + E_3) + \text{c.c.}$ Variations of W_4 and T_4 for different values of r are shown in [figure 7](#).

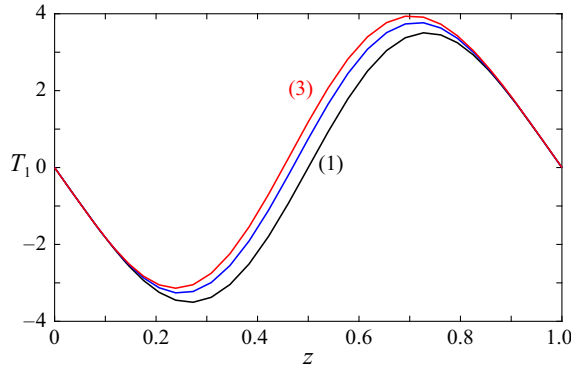


FIGURE 4. Modification of the conductive temperature profile at $Pr = 50$ and different values of the viscosity ratio: (1) $r = 1$; (2) $r = 2$ and (3) $r = 3$.

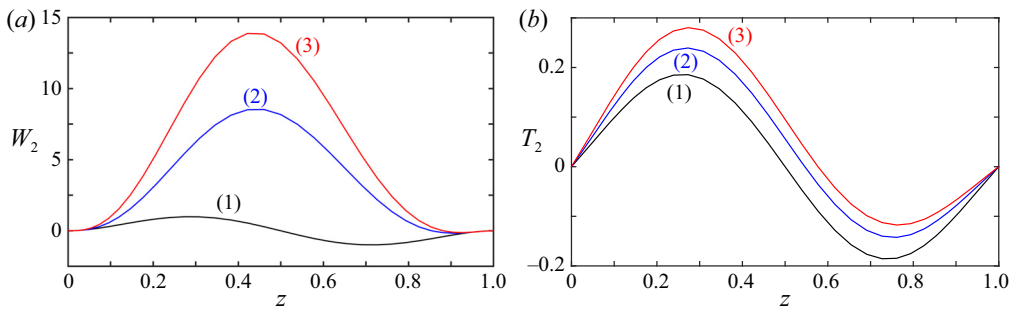


FIGURE 5. First harmonic of the fundamental at $Pr = 50$ and different values of the viscosity ratio: (1) $r = 1$; (2) $r = 2$ and (3) $r = 3$.

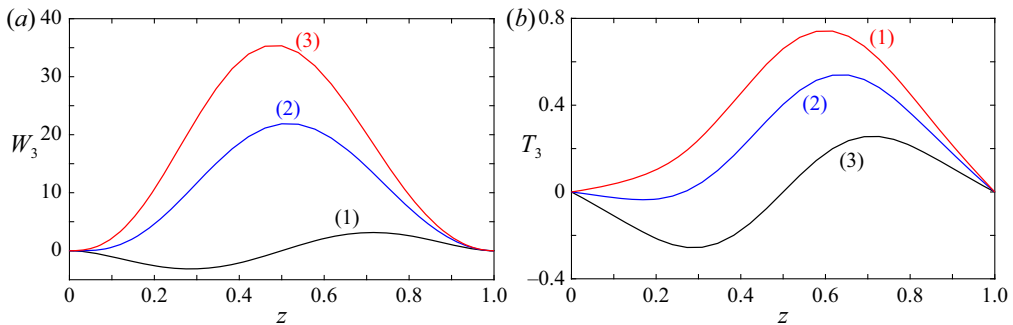


FIGURE 6. Modes factor of $A_p A_q^* \exp(i(k_p - k_q))$ at $Pr = 50$ and different values of r : (1) $r = 1$; (2) $r = 2$ and (3) $r = 3$.

4.3. Solution at order δ^3

At this order, we obtain the equation for the evaluation of $\Psi^{(3)}$:

$$L^{(0)}\Psi^{(3)} = M^{(0)}\frac{\partial\Psi^{(1)}}{\partial T} - L^{(1)}\Psi^{(2)} - L^{(2)}\Psi^{(1)} - NI^{(3)} - NV^{(3)}. \quad (4.19)$$

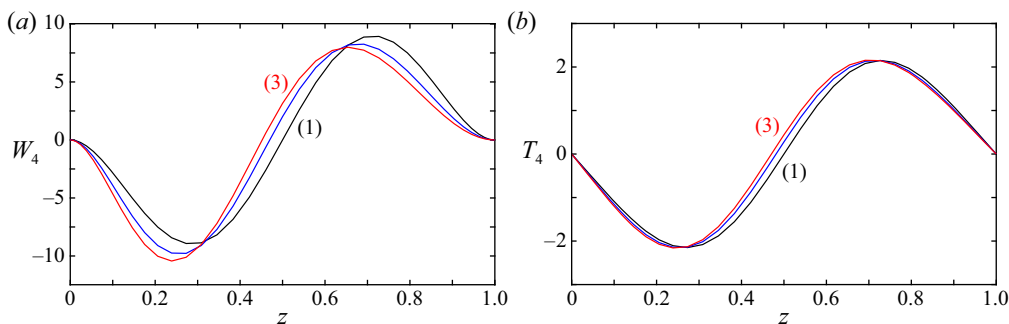


FIGURE 7. Modes factor of $\exp(ik_p \cdot r)$ at $Pr = 50$ and different values of r : (1) $r = 1$; (2) $r = 2$ and (3) $r = 3$.

We need not solve (4.19) but only write the solvability condition to get an equation for $Ra^{(2)}$. To obtain the amplitude equations at cubic order, we use (4.6) combined with $\epsilon = (Ra - Ra_c)/Ra_c$, the departure from the linear threshold. We have

$$\epsilon A_1 = \frac{\delta}{Ra_c} Ra^{(1)} A_1 + \frac{\delta^2}{Ra_c} Ra^{(2)} A_1. \tag{4.20}$$

We substitute in (4.20) $Ra^{(1)} A_1$ and $Ra^{(2)} A_1$ by their expressions derived from the solvability conditions at orders δ^2 and δ^3 , i.e. (4.18) and (D 7) in appendix D, respectively. Finally, returning to the fast variable $\delta A_j(X, Y, T) = A'_j(x, y, t)$, $\partial/\partial X = (1/\delta)(\partial/\partial x), \dots$, we obtain

$$\begin{aligned} \frac{\partial A_1}{\partial t} = & \frac{\epsilon}{\tau_0} A_1 + \frac{\xi_0^2}{\tau_0} (\mathbf{k}_1 \cdot \nabla_{Hx})^2 A_1 + \zeta A_2^* A_3^* \\ & - g_1 |A_1|^2 A_1 - g_2 (|A_2|^2 + |A_3|^2) A_1 \\ & + i\beta_1 [A_2^* (\mathbf{k}_3 \cdot \nabla_{Hx}) A_3^* + A_3^* (\mathbf{k}_2 \cdot \nabla_{Hx}) A_2^*] \\ & + i\beta_2 [A_2^* (\mathbf{k}_2 \cdot \nabla_{Hx}) A_3^* + A_3^* (\mathbf{k}_3 \cdot \nabla_{Hx}) A_2^*], \end{aligned} \tag{4.21}$$

where ∇_{Hx} is the horizontal gradient for the fast variables. Companion equations for A_2 and A_3 are obtained by subindex permutation. In the above equations we have dropped the prime in A'_j and we expect no confusion to the reader.

Following Echebarría & Pérez-García (1998), it is useful to express the derivatives in (4.21) in terms of unitary vectors of the corresponding mode: $\mathbf{n}_2 = -\mathbf{n}_3/2 + (\sqrt{3}/2)\boldsymbol{\tau}_3$ in the term $A_2^* (\mathbf{k}_2 \cdot \nabla_{Hx}) A_3^*$ and $\mathbf{n}_3 = -\mathbf{n}_2/2 - (\sqrt{3}/2)\boldsymbol{\tau}_2$ in the term $A_3^* (\mathbf{k}_3 \cdot \nabla_{Hx}) A_2^*$, where \mathbf{n}_i is the unitary vector in the direction of \mathbf{k}_i and $\boldsymbol{\tau}_i$ orthogonal to \mathbf{n}_i . We obtain

$$\begin{aligned} \frac{\partial A_1}{\partial t} = & \frac{\epsilon}{\tau_0} A_1 + \frac{\xi_0^2}{\tau_0} (\mathbf{n}_1 \cdot \nabla_{Hx})^2 A_1 + \zeta A_2^* A_3^* \\ & - g_1 |A_1|^2 A_1 - g_2 (|A_2|^2 + |A_3|^2) A_1 \\ & + i\alpha_1 [A_2^* (\mathbf{n}_3 \cdot \nabla_{Hx}) A_3^* + A_3^* (\mathbf{n}_2 \cdot \nabla_{Hx}) A_2^*] \\ & + i\alpha_2 [A_2^* (\boldsymbol{\tau}_3 \cdot \nabla_{Hx}) A_3^* + A_3^* (\boldsymbol{\tau}_2 \cdot \nabla_{Hx}) A_2^*]. \end{aligned} \tag{4.22}$$

As indicated by Bragard & Velarde (1998) and Brand (1989), there is no Lyapunov functional for (4.22), opening the possibility for complex spatio-temporal behaviour and

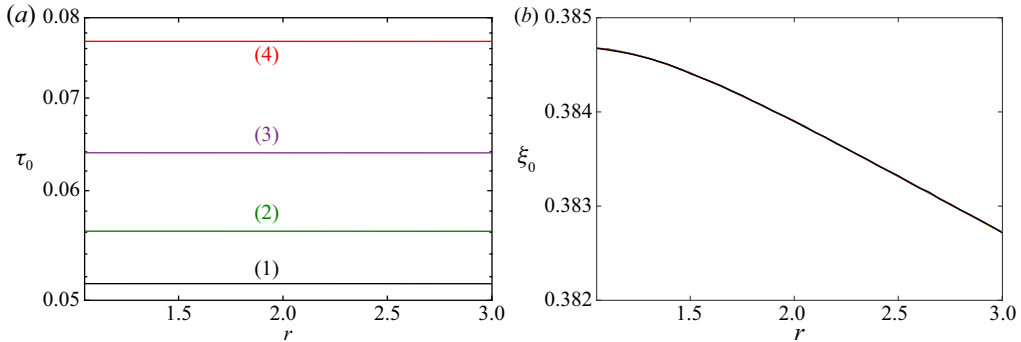


FIGURE 8. Variation of the characteristic time τ_0 (a) and the coherence length ξ_0 (b) as a function of the viscosity ratio, for different values of Prandtl number. (1) $Pr = 50$; (2) $Pr = 5$; (3) $Pr = 2$; (4) $Pr = 1$.

it is possible, for some values of α_1 and α_2 , that the steady state cannot be reached. In contrast, when α_1 and α_2 vanish, a Lyapunov functional can be written down in the form

$$\frac{\partial A_j}{\partial t} = -\frac{\partial \mathcal{F}}{\partial A_j^*}, \quad (4.23)$$

with

$$\begin{aligned} \mathcal{F} = & \iint \sum_{j=1}^3 \left[-\frac{\epsilon}{\tau_0} |A_j|^2 + \frac{\xi_0^2}{\tau_0} |(\mathbf{n}_j \cdot \nabla_{H_x}) A_j|^2 + \frac{g_1}{2} |A_j|^4 \right] dx dy \\ & + g_2 [|A_1|^2 |A_2|^2 + |A_1|^2 |A_3|^2 + |A_2|^2 |A_3|^2] - \zeta (A_1 A_2 A_3 + \text{c.c.}). \end{aligned} \quad (4.24)$$

This functional \mathcal{F} guarantees that only stationary patterns (given in the following section) are possible as $t \rightarrow \infty$.

The characteristic time for the instability to grow τ_0 and the coherence length ξ_0 are shown in figure 8 as a function of r and for different values of Pr . As it can be observed, τ_0 decreases with increasing Prandtl number. Nevertheless, there is no significant effect from $Pr = 50$. Furthermore, the viscosity ratio r has practically no influence on τ_0 at least for $r \in [1, 3]$. Concerning the coherence length ξ_0 , the curves determined at different values of Pr collapse onto a master curve where ξ_0 decreases slightly with increasing r . The coefficient ζ arises from non-Oberbeck–Boussinesq effects. It increases with increasing viscosity ratio, since $\zeta \propto c = \ln(r)$, and with increasing Prandtl number as it is shown in figure 9. However, it is observed that from $Pr = 50$, there is no significant effect of Pr . The coefficient g_1 refers to the self-saturation coefficient and g_2 the cross-saturation coefficient. It can be shown straightforwardly that g_1 and g_2 can be written as the sum of two contributions. The first one (g_1^N, g_2^N) similar to that obtained for a Newtonian fluid arises from the nonlinear inertial terms and the thermodependency of the viscosity. The second contribution (g_1^V, g_2^V) arises from the nonlinear variation of the viscosity with the shear rate

$$g_1 = g_1^N + g_1^V \quad \text{with } g_1^V = -\alpha g_1^{NV}, \quad (4.25)$$

and similarly for g_2 . Variations of g_1^N, g_1^{NV}, g_2^N and g_2^{NV} as a function of the viscosity ratio for different values of Pr are displayed in figure 10. The coefficients g_1 and g_2 increase

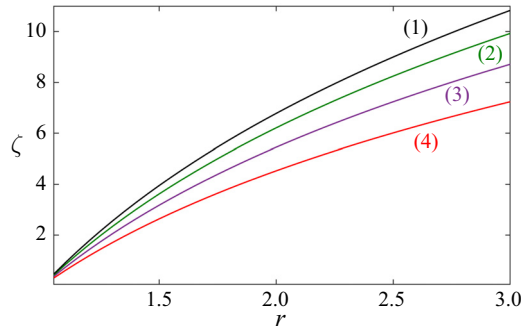


FIGURE 9. Variation of ζ with the ratio viscosity r for different values of the Prandtl number. (1) $Pr = 50$; (2) $Pr = 5$; (3) $Pr = 2$; (4) $Pr = 1$.

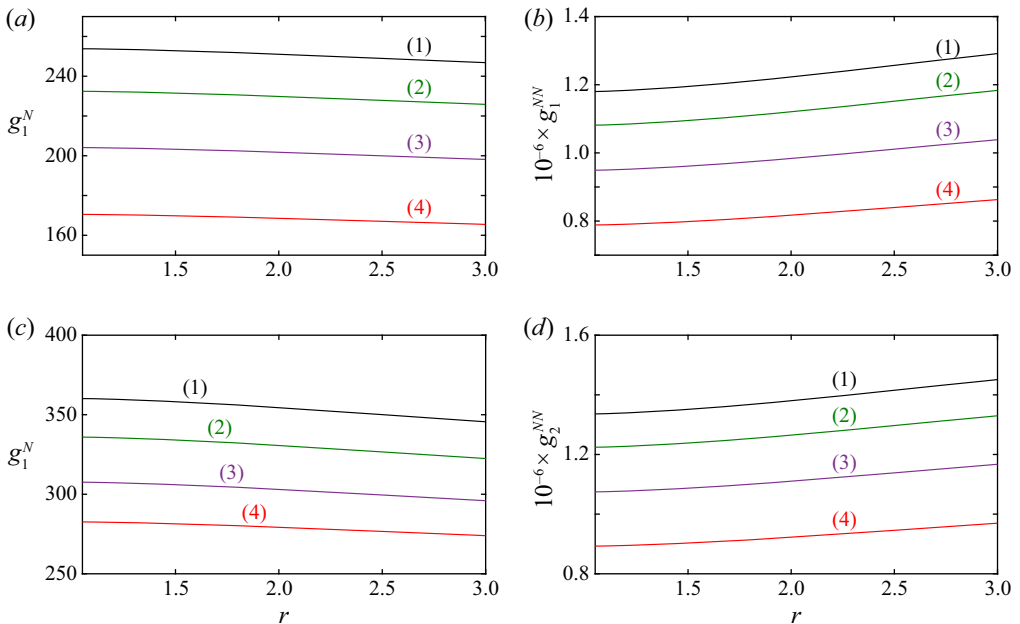


FIGURE 10. (a) ‘Newtonian’ and (b) non-Newtonian contribution to the first Landau coefficient and to the cross-saturation coefficient (c) and (d), respectively, as a function of r for different values of Pr . (1) $Pr = 50$; (2) $Pr = 5$; (3) $Pr = 2$; (4) $Pr = 1$.

significantly with the Prandtl number up to $Pr = 50$, whereas their dependency on r is quiet modest. The coefficients α_1 and α_2 , displayed in figure 11, are real. The term with α_1 accounts for distortions in the directions of rolls and, therefore, corresponds physically to wavenumber dilatation. The coefficient α_1 is positive and takes values of the same order as ζ . Note also that α_1 vanishes when $r = 1$, and increases with increasing r . The terms with α_2 account for distortions in the hexagonal form. The coefficient α_2 is negative and smaller (in absolute value) than α_1 . Following Echebarria & Perez-Garcia (2001), a sketch of their action is drawn in figure 12.

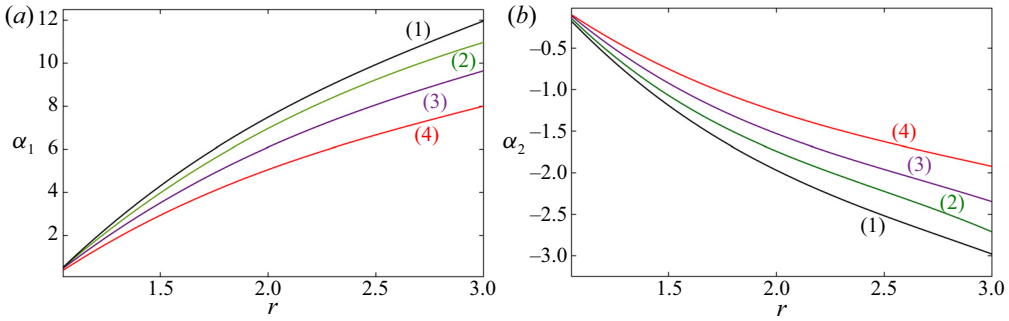


FIGURE 11. Coefficients α_1 and α_2 as a function of r for different values of Pr . (1) $Pr = 50$; (2) $Pr = 5$; (3) $Pr = 2$; (4) $Pr = 1$.

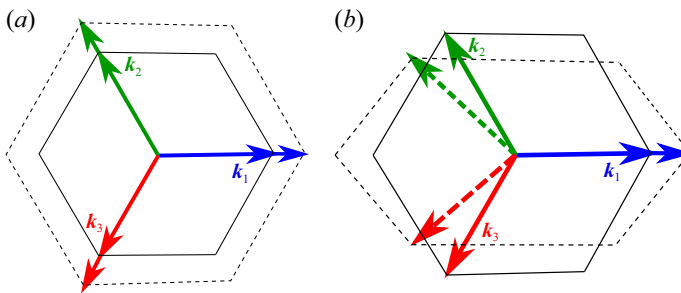


FIGURE 12. (a) Dilatation and (b) distortion of hexagonal pattern (Echebarria & Perez-Garcia 2001).

For the set of coefficients discussed above, the following correlations can be used:

$$\left. \begin{aligned}
 \tau_0 &= 0.0509 + 0.026Pr^{-1}; & \xi_0 &= 0.385 - 3.57 \times 10^{-4}r - 1.68 \times 10^{-4}r^2, \\
 \zeta &= (9.90 - 4.72Pr^{-1} + 1.38Pr^{-2}) \log(r), \\
 g_1^N &= 254.3(1.0037 - 0.4722Pr^{-1} + 0.1392Pr^{-2})(1.0067 - 0.0037r - 0.002r^2), \\
 g_1^{NN} &= 11.86 \cdot 10^5(1.0038 - 0.4808Pr^{-1} + 0.1422Pr^{-2})(0.9733 + 0.0128r + 0.0094r^2), \\
 g_2^N &= 375.9(1.0029 - 0.3545Pr^{-1} + 0.1020Pr^{-2})(1.0091 - 0.0047r - 0.0029r^2), \\
 g_2^{NN} &= 1.343 \cdot 10^6(1 - 0.476Pr^{-1} + 0.146Pr^{-2})(0.9756 + 0.0117r + 0.0086r^2), \\
 \alpha_1 &= 12.5(1 - 0.504Pr^{-1} + 0.148Pr^{-2}) \log(r), \\
 \alpha_2 &= -2.1(1.003 - 0.238Pr^{-1} + 0.069Pr^{-2}) \log(r).
 \end{aligned} \right\} (4.26)$$

5. Competition between rolls and squares

It was shown theoretically by Busse & Frick (1985) and Jenkins (1987), and experimentally by White (1988), that at low values of the viscosity ratio r , rolls are the preferred pattern of convection, whereas squares are the preferred for larger values of r . For a Newtonian fluid with an exponential viscosity function, Jenkins (1987) found that the changeover to squares occurs at $r_\ell \approx 3.2$. In this section we investigate the influence of

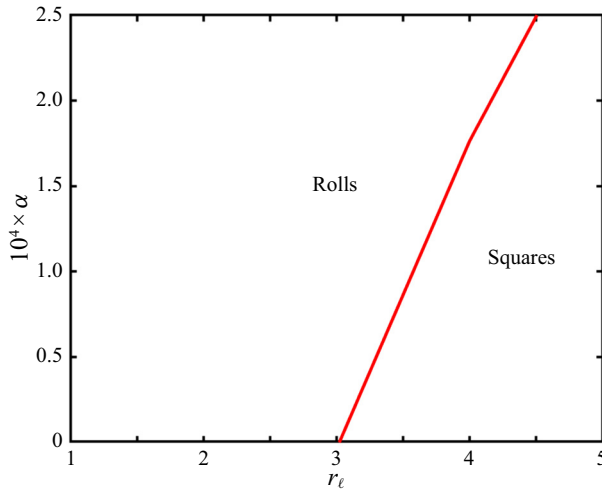


FIGURE 13. Domains of stability of rolls and squares in the plane (α, r_ℓ) .

shear-thinning effects on this limit value r_ℓ . Here, we consider only competition between perfect rolls and squares without spatial modulation. In a square lattice the solution at order δ is

$$w^{(1)} = F_{11}(z)[A_1 \exp(i\mathbf{k}_1 \cdot \mathbf{r}) + A_2 \exp(i\mathbf{k}_2 \cdot \mathbf{r})] + \text{c.c.}, \tag{5.1}$$

$$\theta^{(1)} = G_{11}(z)[A_1 \exp(i\mathbf{k}_1 \cdot \mathbf{r}) + A_2 \exp(i\mathbf{k}_2 \cdot \mathbf{r})] + \text{c.c.} \tag{5.2}$$

The derivation of amplitude equations without spatial terms for the two modes A_1 and A_2 forming an angle of 90° follows the same procedure as in § 4. They are given by

$$\frac{dA_1}{dt} = sA_1 - [g_1|A_1|^2 + g_{2s}|A_2|^2]A_1 + \dots, \tag{5.3}$$

$$\frac{dA_2}{dt} = sA_2 - [g_1|A_2|^2 + g_{2s}|A_1|^2]A_2 + \dots \tag{5.4}$$

Note that (5.3), (5.4) can be obtained using symmetries introduced by the square lattice: symmetries of square D_4 in addition to the two-torus T_2 of translation in the two horizontal directions (Golubitsky, Swift & Knoblock 1984; McKenzie 1988).

A linear stability analysis of stationary rolls and squares, i.e. stationary solutions of (5.3), (5.4) is performed. It is shown that squares are stable when $g_{2s} < g_1$, i.e. when the cross-coupling between two orthogonal modes that describe the square pattern is weak enough. The numerical results are displayed in figure 13 where we have represented the variation of r_ℓ as a function of the shear-thinning degree α at $Pr = 10$. On the left of the curve, rolls are stable and on the right of the curve, squares are stable. One note is that r_ℓ increases with increasing shear-thinning effects.

6. Amplitude instabilities

In this section we consider homogeneous and stationary solutions of (4.22) by including a slightly off-critical wavenumber in the amplitude ($A_p = \mathcal{A}_p \exp(i\mathbf{q}_p \cdot \mathbf{r})$). We discuss

their domain of existence and their stability with respect to homogeneous perturbations (amplitude instabilities).

(i) Roll solution with a wavenumber slightly off-critical $k = k_c + q$. It is given by $A_1 = R_0 \exp(iqx)$, $A_2 = A_3 = 0$, and any circular permutation with $R_0 = \sqrt{(\epsilon - \xi_0^2 q^2)/\tau_0 g_1}$. A linear stability analysis of this solution with respect to uniform perturbations $A_1 = (R_0 + r_1) \exp(iqx_1)$, $A_2 = r_2 \exp(iqx_2)$ and $A_3 = r_3 \exp(iqx_3)$, where $x_p = \mathbf{n}_p \cdot \mathbf{r}$ with $p = 1, 2, 3$, shows that the roll solution is stable when $g_2 > g_1$ and

$$\epsilon > \epsilon_r(q) = \frac{\tau_0 g_1 (\zeta + 2\alpha_1 q)^2}{(g_2 - g_1)^2} + \xi_0^2 q^2. \tag{6.1}$$

(ii) Hexagon solutions: three sets of rolls of equal amplitude, $A_p = H_0 \exp(i q x_p)$ with

$$H_0 = \frac{(\zeta + 2\alpha_1 q) + \sqrt{(\zeta + 2\alpha_1 q)^2 + 4(g_1 + 2g_2)(\epsilon - \xi_0^2 q^2)/\tau_0}}{2(g_1 + 2g_2)}, \tag{6.2}$$

called up-hexagons, that correspond to upflow in the centre, and

$$H_0 = \frac{-\zeta - 2\alpha_1 q + \sqrt{(\zeta + 2\alpha_1 q)^2 + 4(\epsilon - \xi_0^2 q^2)(g_1 + 2g_2)/\tau_0}}{2(g_1 + 2g_2)}, \tag{6.3}$$

called down-hexagons, that correspond to downflow motion in the centre.

Solutions called up-hexagons, exist for

$$\epsilon > \epsilon_a = -\frac{(\zeta + 2\alpha_1 q)^2 \tau_0}{4(g_1 + 2g_2)} + \xi_0^2 q^2, \tag{6.4}$$

and are linearly stable for $\epsilon_a < \epsilon < \epsilon_h$, with

$$\epsilon_h = \frac{\tau_0(\zeta + 2\alpha_1 q)^2(2g_1 + g_2)}{(g_1 - g_2)^2} + \xi_0^2 q^2. \tag{6.5}$$

Note that ϵ_a and ϵ_h do not contain α_2 since only perfect hexagons are considered.

Solutions called down-hexagons, exist for $\epsilon > \xi_0^2 q^2$ and are linearly unstable.

(iii) The ‘mixed states’ given by

$$A_1 = \frac{\zeta - 2\alpha_1 q}{g_2 - g_1}, \quad A_2 = A_3 = \sqrt{\frac{(\epsilon - \xi_0^2 q^2)/\tau_0 - g_1 A_1^2}{g_1 + g_2}} \tag{6.6}$$

and any circulation permutation exist for $\epsilon > (\zeta + 2\alpha_1 q)^2 g_1 / (g_1 - g_2)^2 + \xi_0^2 \tau_0$ and are linearly unstable with respect to rolls or up-hexagons.

An example of amplitude stability curves in (ϵ, q) space and the associated bifurcation diagram for $q = 0$ is given in figures 14 and 15. Hexagons bifurcate transcritically from the conductive state where they are unstable. Both hexagons and the conductive state are stable in the range $\epsilon_a \leq \epsilon \leq 0$ and both hexagons and rolls are stable in the range $\epsilon_r \leq \epsilon \leq \epsilon_h$. In this range, rolls and hexagons are linked via a branch of mixed modes which are always unstable.

Variations of ϵ_a , ϵ_r , ϵ_h and $(\epsilon_h - \epsilon_r)$ as a function of the viscosities ratio, r , for different values of the shear-thinning degree are depicted in figure 16. Overall, the

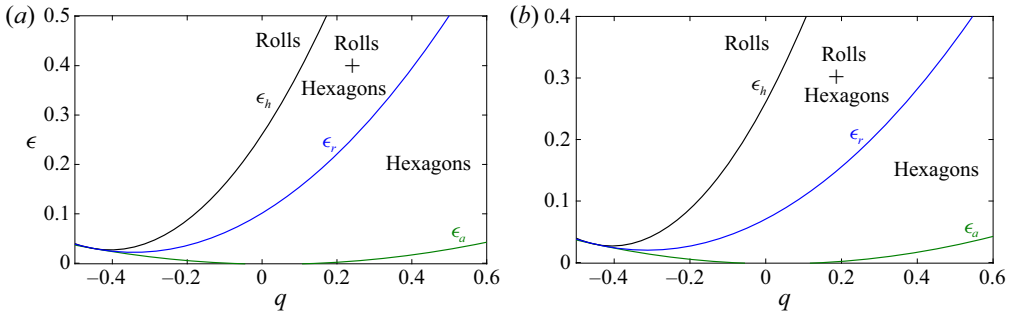


FIGURE 14. Amplitude stability curves in the (ϵ, q) plane at $r = 2.5, Pr = 50$ and two different values of α : (a) $\alpha = 0$ Newtonian fluid, (b) $\alpha = 10^{-4}$ Carreau fluid.

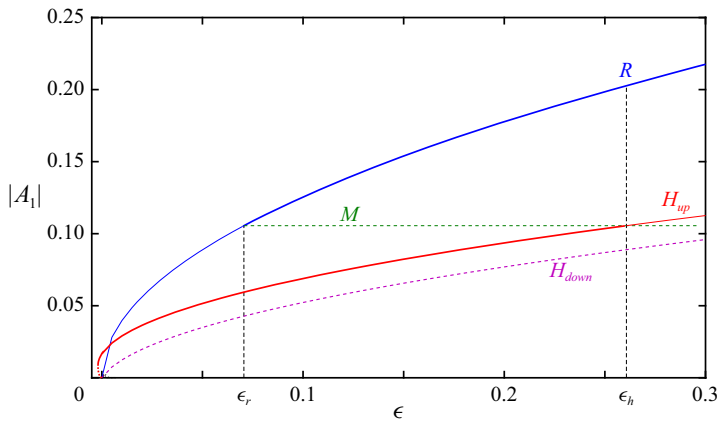


FIGURE 15. Bifurcation diagram for hexagons in the case where $g_2 > g_1$ with the parameters $r = 2.5, q = 0$ and $\alpha = 10^{-4}$. The amplitude $|A_1|$ is plotted against the distance to the threshold ϵ for the roll-solution branch (labelled R), for the mixed mode branch (labelled M) and for the two hexagon-solution branches, up- and down-hexagons. Solid lines indicate stable solutions and dashed lines represent unstable solutions.

thermdependency of the viscosity favours convection in the form of hexagons and their stability whereas shear-thinning effects favour convection in form of rolls and their stability. For instance, in figure 16(c) the domain of stability of hexagons increases with increasing r and decreases with increasing shear-thinning effects. In the same way, in figure 16(d) the domain of bistability rolls and hexagons shrinks with increasing α , and increases with increasing the viscosities ratio, i.e. the thermdependency effect. One can also note in figure 16(a) that $|\epsilon_a|$ increases with increasing α as shear-thinning effects favour a subcritical bifurcation (Bouteraa *et al.* 2015). The correlations proposed by Busse (1967) for a Newtonian fluid assuming a linear variation of the viscosity with temperature (see appendix E) are displayed for comparison. As it can be observed, the difference between the linear and the exponential models increases with increasing r .

7. Phase instabilities

In this section we consider perturbations involving spatial modulations over distances much larger than the basic wavelength. The amplitudes of slightly distorted up-hexagons

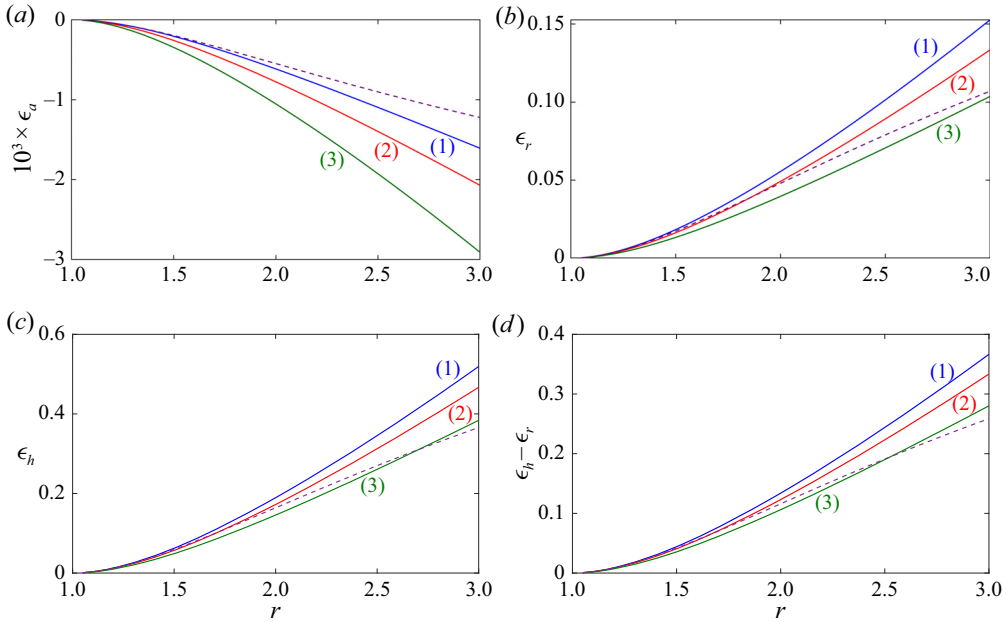


FIGURE 16. Variations of ϵ_a , ϵ_r , ϵ_h and $(\epsilon_h - \epsilon_r)$ versus r for three values of the shear-thinning degree α . The Prandtl number is fixed, $Pr = 50$. (1) Newtonian fluid, $\alpha = 0$; (2) Carreau fluid with $\alpha = 0.5 \cdot 10^{-4}$; (3) Carreau fluid with $\alpha = 10^{-4}$. The dashed line is the correlation proposed par Busse (1967) for a Newtonian fluid, assuming a linear variation of the viscosity with temperature.

can be written as

$$A_p = (H_0 + r_p) \exp [i(qx_p + \phi_p)], \quad p = 1, 2, 3, \tag{7.1}$$

where $x_p = \mathbf{n}_p \cdot \mathbf{r}$. Here, A_p represents the amplitude of a slightly distorted hexagonal pattern, $|r_p(x_1, x_2, x_3, t)| \ll 1$ and $|\phi_p(x_1, x_2, x_3, t)| \ll 1$ are the amplitude and the phase of the perturbation, respectively. Substitution of (7.1) into (4.22) and linearizing with respect to r_p and ϕ_p leads to the following set of equations:

$$\begin{aligned} \frac{\partial r_p}{\partial t} = & -[2g_1 H_0 + (\zeta + 2\alpha_1 q)] H_0 r_p + \frac{\xi_0^2}{\tau_0} \frac{\partial^2 r_p}{\partial x_p^2} \\ & + [(\zeta + 2\alpha_1 q) - 2g_2 H_0] H_0 (r_j + r_k) - 2q H_0 \frac{\xi_0^2}{\tau_0} \frac{\partial \phi_p}{\partial x_p} \\ & + \left(\alpha_1 + \frac{\alpha_2}{\sqrt{3}} \right) H_0^2 \left(\frac{\partial \phi_j}{\partial x_j} + \frac{\partial \phi_k}{\partial x_k} \right) + \frac{2\alpha_2}{\sqrt{3}} H_0^2 \left(\frac{\partial \phi_j}{\partial x_k} + \frac{\partial \phi_k}{\partial x_j} \right), \end{aligned} \tag{7.2}$$

$$\begin{aligned} \frac{\partial \phi_p}{\partial t} = & -(\zeta + 2\alpha_1 q) H_0 (\phi_p + \phi_j + \phi_k) + \frac{\xi_0^2}{\tau_0} \frac{\partial^2 \phi_p}{\partial x_p^2} + \frac{2q}{H_0} \frac{\xi_0^2}{\tau_0} \frac{\partial r_p}{\partial x_p} \\ & + \left(\alpha_1 + \frac{\alpha_2}{\sqrt{3}} \right) \left(\frac{\partial r_j}{\partial x_j} + \frac{\partial r_k}{\partial x_k} \right) + \frac{2\alpha_2}{\sqrt{3}} \left(\frac{\partial r_j}{\partial x_k} + \frac{\partial r_k}{\partial x_j} \right). \end{aligned} \tag{7.3}$$

In the long wavelength limit the perturbations r_p in the amplitudes follow adiabatically the phase dynamics and are eliminated with the total phase $\Phi = \phi_1 + \phi_2 + \phi_3$. As a result, only two phases dominate the dynamics of the modulated hexagonal pattern. Instead of using ϕ_2 and ϕ_3 it is convenient to consider $\phi_x = -(\phi_2 + \phi_3)$ and $\phi_y = (1/\sqrt{3})(\phi_2 + \phi_3)$, which are related to the two translational symmetries in the x and y directions, respectively (Echebarría & Pérez-García 1998; Echebarria & Perez-Garcia 2001). The resulting equations can then be written as a linear diffusion equation of the phase vector $\phi = (\phi_x, \phi_y)$,

$$\frac{\partial \phi}{\partial t} = D_{\perp} \nabla^2 \phi + (D_{\parallel} - D_{\perp}) \nabla (\nabla \cdot \phi), \tag{7.4}$$

where D_{\perp} and D_{\parallel} are the transverse and longitudinal phase diffusion coefficients, given by

$$D_{\perp} = \frac{1}{4} \frac{\xi_0^2}{\tau_0} - \frac{q^2}{2\tilde{u}} \left(\frac{\xi_0^2}{\tau_0} \right)^2 + \frac{H_0^2}{8\tilde{u}} \left(\alpha_1 - \sqrt{3} \alpha_2 \right)^2, \tag{7.5}$$

$$D_{\parallel} = \frac{3}{4} \frac{\xi_0^2}{\tau_0} - \frac{q^2 (4\tilde{u} + \tilde{v})}{2\tilde{u}\tilde{v}} \left(\frac{\xi_0^2}{\tau_0} \right)^2 + \frac{H_0^2}{8\tilde{u}} \left(\alpha_1 - \sqrt{3} \alpha_2 \right)^2 - \frac{H_0^2 \alpha_1}{\tilde{v}} \left(\alpha_1 + \sqrt{3} \alpha_2 \right) + \frac{H_0 q \xi_0^2}{\tilde{v} \tau_0} \left(3\alpha_1 + \sqrt{3} \alpha_2 \right), \tag{7.6}$$

with

$$\tilde{u} = H_0^2 (g_1 - g_2) + (\zeta + 2\alpha_1 q) H_0, \tag{7.7}$$

$$\tilde{v} = 2H_0^2 (g_1 + 2g_2) - (\zeta + 2\alpha_1 q) H_0. \tag{7.8}$$

Note that both \tilde{u} and \tilde{v} have to be positive for hexagons to be stable against amplitude instabilities. The phase equation (7.4) allows us to split the phase vector ϕ into longitudinal ϕ_{ℓ} and transverse ϕ_t modes, $\phi = \phi_{\ell} + \phi_t$, that satisfy $\nabla \times \phi_{\ell} = 0$ and $\nabla \cdot \phi_t = 0$, respectively. This leads to the uncoupled phase diffusion equations (Lauzeral, Metens & Walgraef 1993; Echebarría & Pérez-García 1998; Echebarria & Perez-Garcia 2001; Pena & Perez-Garcia 2001)

$$\frac{\partial \phi_{\ell}}{\partial t} = D_{\parallel} \nabla^2 \phi_{\ell}, \quad \frac{\partial \phi_t}{\partial t} = D_{\perp} \nabla^2 \phi_t. \tag{7.9a,b}$$

The normal modes ϕ_t and ϕ_{ℓ} correspond to Eckhaus rectangular and rhomboidal perturbations, respectively. The hexagons are stable to phase modes in the domain defined by $D_{\parallel} > 0$ and $D_{\perp} > 0$. In the figure 17 we show the phase stability diagrams for a Newtonian fluid and two different values of the viscosities ratio r . Curves (1) and (2) correspond to $D_{\perp} = 0$ and $D_{\parallel} = 0$, respectively. Curve (4) is the upper stability amplitude where a bifurcation to rolls occurs. The minimum of curve (4) is located in the region $q < 0$. Below curve (3), no hexagons exist. Hexagons are stable in the shaded region. For viscosities ratio $1 \leq r \leq 2$, the region of stability to amplitude and phase modes is closed. Whereas for larger values of r , the stability domain is open. Note also that the domain of stability is decentred towards the right. It is delimited mainly by the stability amplitude curves and the transverse phase instability boundary. Nevertheless, the numerical results show that close to the threshold, the longitudinal mode is the relevant destabilizing mode. The region where the longitudinal mode destabilizes the pattern increases slightly with

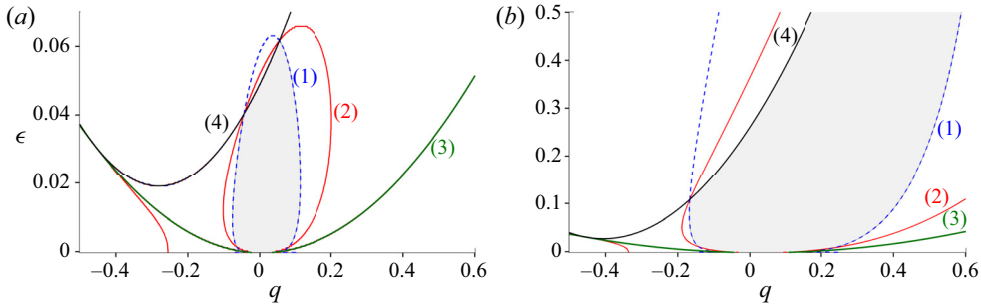


FIGURE 17. Hexagon stability diagram for a Newtonian fluid at $Pr = 50$ and two different values of the viscosities ratio: (a) $r = 1.5$ and (b) $r = 2.5$. Hexagons are stable inside the grey area. Curve (1): $D_{\perp} = 0$, curve (2) $D_{\parallel} = 0$, curve (3) bifurcation from the conductive state to convection with hexagons, curve (4) bifurcation from hexagons to rolls.

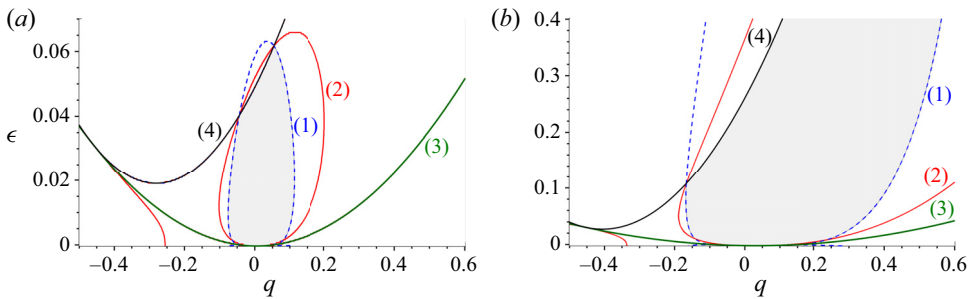


FIGURE 18. Hexagon stability diagram for a shear-thinning fluid with $\alpha = 10^{-4}$ at $Pr = 50$ and two different values of the viscosities ratio: (a) $r = 1.5$ and (b) $r = 2.5$. Hexagons are stable inside the grey area.

increasing r . Qualitatively, a similar description of the phase stability diagram can be done for a Carreau fluid with low or moderate values of r as it is shown in figure 18. Once again, the region where the longitudinal mode is the relevant destabilizing mode remains small and close to the onset. A summary of the results relating to the influence of r and α on the stability domain of hexagons is given by figure 19(a). With increasing shear-thinning effects, the stability domain becomes more decentred towards the right. Concerning the influence of r , as discussed before, the thermodependency of the fluid viscosity increases significantly the stability domain of hexagons. For comparison, we have represented in figure 19(b) the stability domain of hexagons when $\alpha_1 = \alpha_2 = 0$. This domain is symmetrical with respect to the vertical axis.

8. Numerical solutions of amplitude equations

8.1. Numerical simulation

For numerical integration of the Ginzburg–Landau equations (4.22), we employed a Fourier pseudospectral method on a square mesh with periodic boundary conditions. Calculations are carried out in spectral space (wavenumber) with the exception of evaluating nonlinear and conjugate terms which are performed in physical space. The square domain $[-L/2, L/2] \times [-L/2, L/2]$ is discretized into $N \times N$ uniformly spaced grid points $M_{\ell,p}$ with $x_{\ell} = -L/2 + \ell \Delta x$ (similarly for y_p), $\Delta_x = \Delta_y = L/N$ and N even.

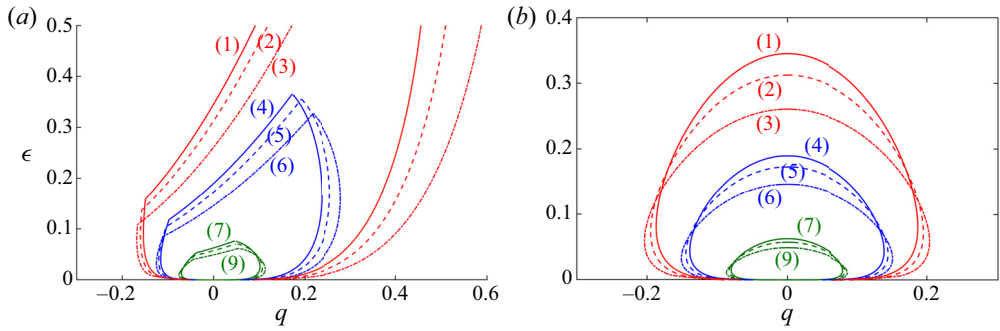


FIGURE 19. Influence of shear-thinning effects and viscosities ratio on the hexagons stability diagram at $Pr = 50$. (a) Spatial non-variational terms in (4.22) are taken into account, (b) $\alpha_1 = \alpha_2 = 0$. Curves (1), (4) and (7) correspond to a Newtonian fluid and three different values of r : 2.5, 2.0, 1.5, respectively. Curves (2), (5) and (8) correspond to a shear-thinning fluid with $\alpha = 5 \times 10^{-5}$. Curves (3), (6) and (9) correspond to a shear-thinning fluid with $\alpha = 10^{-4}$.

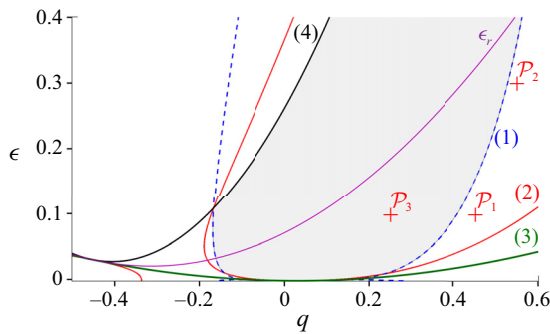


FIGURE 20. Hexagon stability diagram for a shear-thinning fluid with $\alpha = 10^{-4}$, $Pr = 50$ and $r = 2.5$. The curve $\epsilon_r(q)$ is a boundary above which rolls are stable with respect to homogeneous perturbations. (+) Points where numerical simulations were performed.

For the temporal discretization, the time domain $[0, t_{max}]$ is discretized with equal time step of width Δt as $t_m = m\Delta t$, $m = 0, 1, 2, \dots$. The exponential time differencing method of second order (ETD2) proposed by Cox & Matthews (2002) is used. The pseudospectral method is implemented in Matlab. Finally, to check the convergence, several simulations are carried out with an increasing numbers of grid points and refining the time step. For the results presented in this section, the numerical resolution is 512×512 in a square of size $L = 5 \times 2\pi/q$ and the time step is fixed at 0.01.

8.2. Numerical results

Numerical simulations were carried out in order to illustrate the nonlinear evolution of the transverse phase instability for a hexagonal pattern in both cases: (i) low values of ϵ , where practically only hexagons are stable for $q > 0$; and (ii) larger ϵ . We discuss the impact of the non-variational quadratic spatial terms on the competition between rolls and hexagons. Further numerical simulations were done to illustrate the transition rolls-hexagons when $\epsilon < \epsilon_r$. In the following, the results are presented for three values of the parameters (ϵ, q) , represented by the symbol (+) in figure 20.

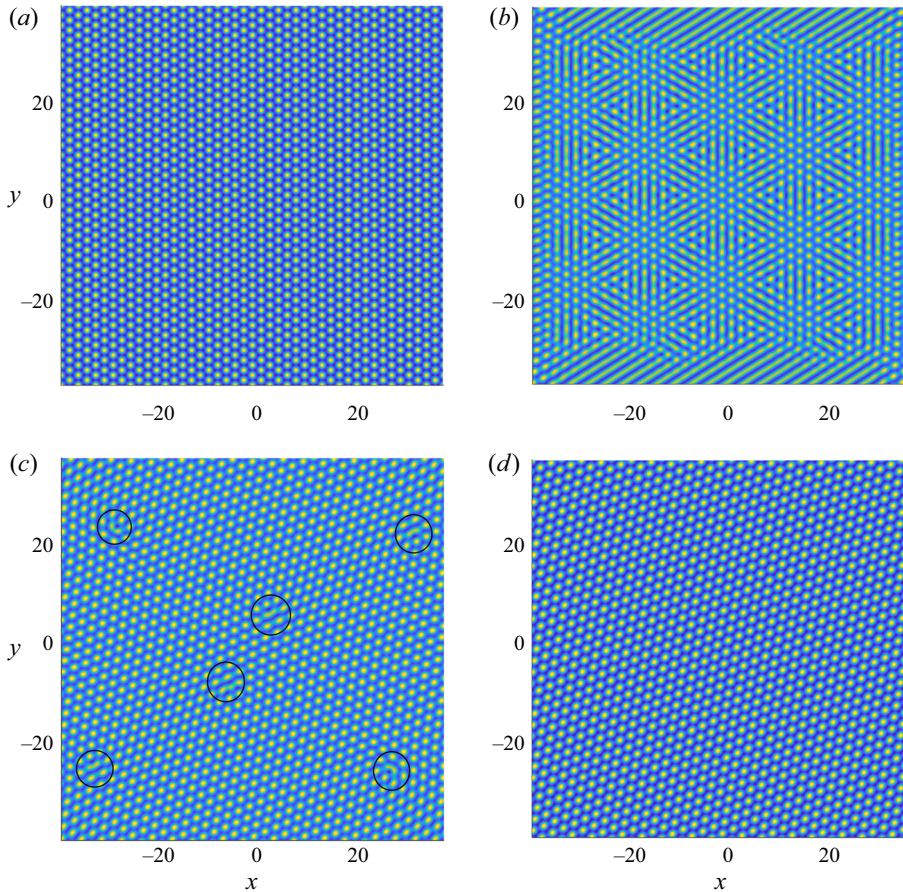


FIGURE 21. Initial condition (\mathcal{P}_1): hexagons with $q = 0.45$, $\epsilon = 0.1$, $r = 2.5$, $\alpha = 10^{-4}$ and $Pr = 50$. Contours of the vertical velocity $w = \sum_{i=1}^3 A_i \exp(i\mathbf{k}_{c,i} \cdot \mathbf{x}) + \text{c.c.}$ for a hexagonal pattern undergoing the transverse instability. The contours are shown at times (a) $t = 0$; (b) $t = 10$; (c) $t = 1000$ and (d) $t = 2000$. In panel (c) the penta-hepta defects are circled.

8.2.1. Nonlinear evolution of the transverse instability at low ϵ

The initial condition is a perfect hexagonal pattern with a wavenumber $k = k_c + 0.45$ at $\epsilon = 0.1$. The point (\mathcal{P}_1), $\epsilon = 0.1$ and $q = 0.45$ in figure 20 is outside the domain where hexagons are stable to phase modes. The other parameters are shear-thinning degree $\alpha = 10^{-4}$, viscosity ratio $r = 2.5$ and Prandtl number $Pr = 50$. At $t = 0$, the hexagonal pattern is slightly disturbed.

Figure 21 displays the time evolution of the vertical velocity $w = \sum_{i=1}^3 A_i(x, y, t) \exp(i\mathbf{k}_{c,i} \cdot \mathbf{r}) + \text{c.c.}$. It shows how the transverse phase instability leads to a stable hexagonal pattern after passing through intermediate stages. The breakdown of the initial pattern takes place through the creation of penta-hepta defects (two hexagons are replaced by a pentagon and a heptagon). At $t = 10$ most of the penta-hepta defects (PHD) are aggregated along lines perpendicular to wavevectors. Their number decreases with time. At $t = 1000$, the number of PHD is quite limited and they are circled in figure 21(c). A zoom is given in figure 22(a). The PHD move and eventually annihilate or disappear at the boundaries. Figure 22 is a focus on one penta-hepta defect. It is shown, figure 22(b–d),

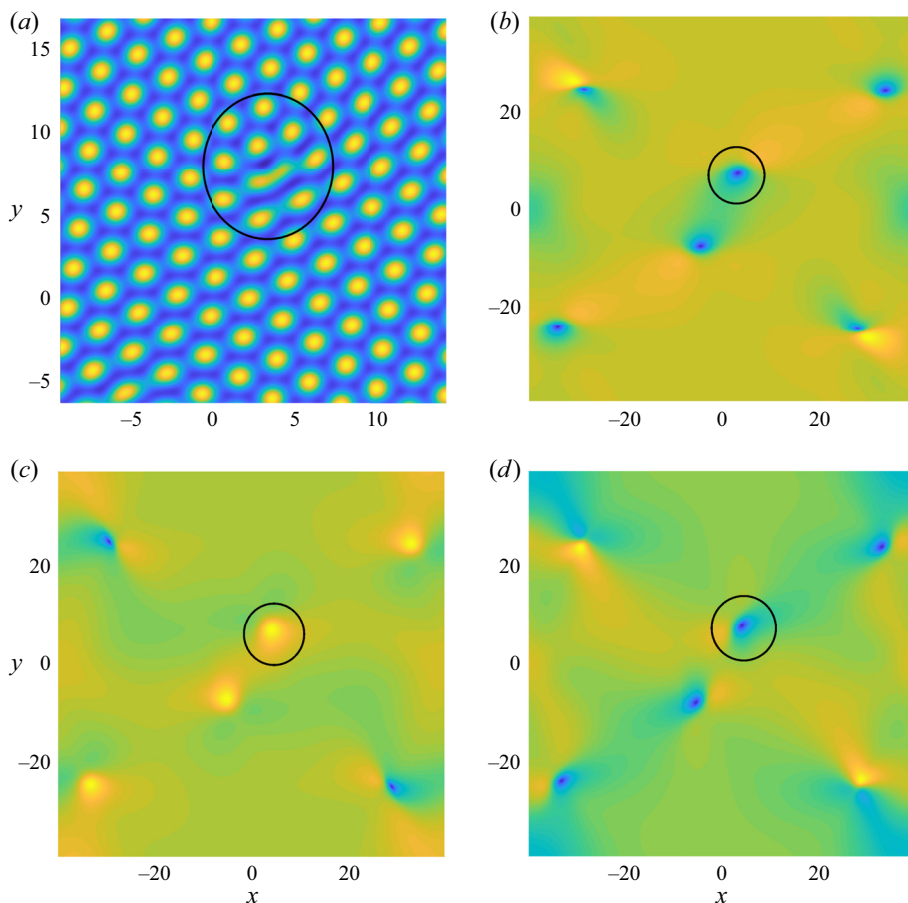


FIGURE 22. Initial condition (\mathcal{P}_1): hexagons with $q = 0.45$, $\epsilon = 0.1$, $r = 2.5$, $\alpha = 10^{-4}$ and $Pr = 50$. Focus on one penta-hepta defect at $q = 0.45$, $r = 2.5$ and $\alpha = 10^{-4}$: (a) contours of the ‘vertical velocity’ w at $t = 1000$ with one penta-hepta defect circled. (b) Modulus of A_1 which vanishes at the core of the defect. (c) Modulus of A_2 , non-zero in the circle ($|A_2| = 0.114$). (d) Modulus of A_3 which vanishes at the core of the defect.

that in this process the amplitude of two of the three rolls making up the hexagonal pattern are zero. The phases of the sets of rolls (obtained from $\arctan(\text{Im}[A_i(x, y)]/\text{Re}[A_i(x, y)])$) are represented in figure 23. The phases of two sets of rolls that vanish at the defect present a singularity, while the third one does not have any singularity. Actually, the penta-hepta defect is pictured as a dislocation in each of the sets of rolls whose amplitude vanishes at the core of the defect (Ciliberto *et al.* 1990; Sushchik & Tsimring 1994; Hoyle 1995).

8.2.2. Nonlinear evolution of the transverse phase instability at large ϵ

In the previous section we considered a rather small ϵ for which hexagons are the only possible state. A completely different final state of the transverse phase instability is observed for larger ϵ , i.e. ϵ greater than a threshold value ϵ^* . Figure 24 shows the nonlinear evolution of the convection pattern when the initial condition, point \mathcal{P}_2 in figure 20, consists of a perfect hexagon at $\epsilon = 0.3$, with a wavenumber, $k = k_c + 0.55$, outside the phase stability domain. The other parameters are $\alpha = 10^{-4}$, $r = 2.5$ and $Pr = 50$. In this case, the transverse phase instability triggers the transition from a regular hexagonal

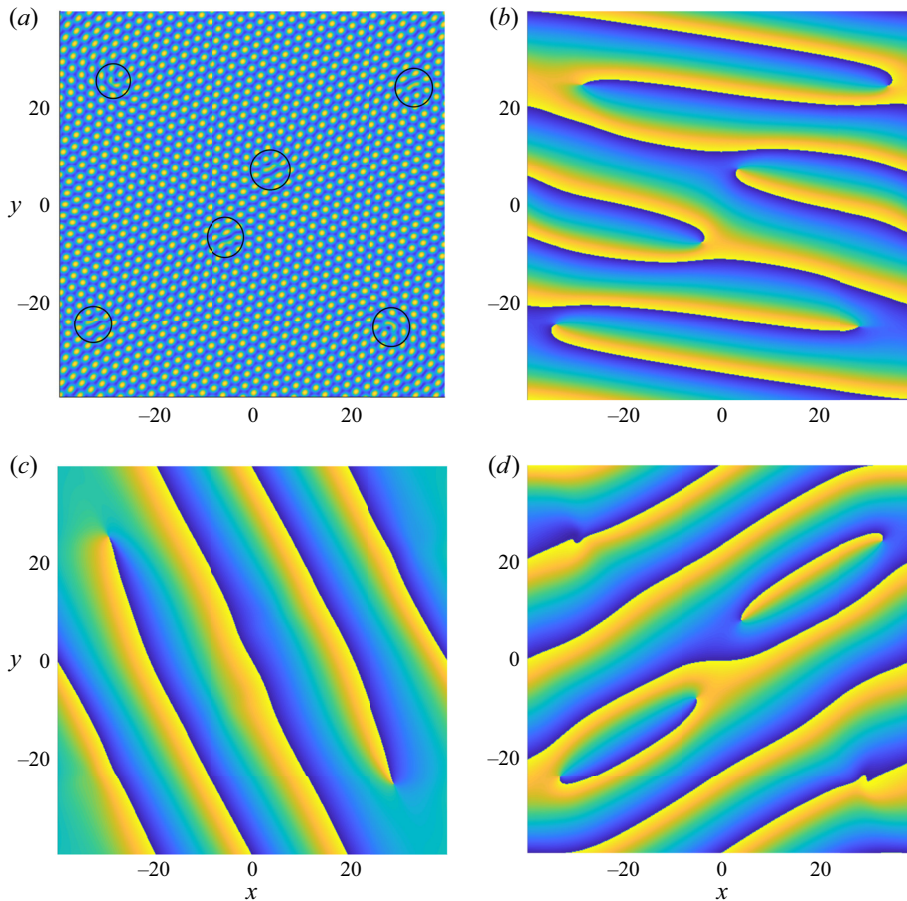


FIGURE 23. Initial condition (\mathcal{P}_1): hexagons with $q = 0.45$, $\epsilon = 0.1$, $r = 2.5$, $\alpha = 10^{-4}$ and $Pr = 50$. (a) Contours of the vertical velocity $w = \sum_{i=1}^3 A_i \exp(\mathbf{i} \mathbf{k}_{c,i} \cdot \mathbf{x}) + \text{c.c.}$ at $t = 1000$; (b) phase of A_1 ; (c) phase of A_2 and (d) phase of A_3 .

pattern to a disordered roll state with several grain boundaries. The threshold value ϵ^* at which the transition to rolls occurs can only be determined by numerical simulations due to the lack of Lyapunov functional for (4.22). For the particular case considered here, $q = 0.55$, $r = 2.5$, $\alpha = 10^{-4}$ and $Pr = 50$, we have found $\epsilon^* \approx 0.22$.

Although at $\epsilon = 0.3$ hexagons are linearly stable to homogeneous perturbations as shown in figure 14(b), when defects first appear, the dynamics may change. According to Sushchik & Tsimring (1994) and Ciliberto *et al.* (1990), the presence of defects in a system plays an important role in the dynamics of transition between rolls and hexagons. In our case, pieces of rolls appear in the beginning. Under certain conditions, they spread and destroy the hexagonal pattern. Furthermore, it is observed that the time necessary to reach the steady state is much lower for large ϵ .

8.2.3. Rolls–hexagons transition

Figure 25 shows the contours of the reconstructed vertical velocity w at different times in the case where the initial data, point \mathcal{P}_3 in figure 20, correspond to perfect rolls at $\epsilon = 0.1$, $q = 0.25$ for a Carreau fluid with $\alpha = 10^{-4}$ and $Pr = 50$. According to figure 14(b), these rolls are unstable. This is confirmed by the computation, in which

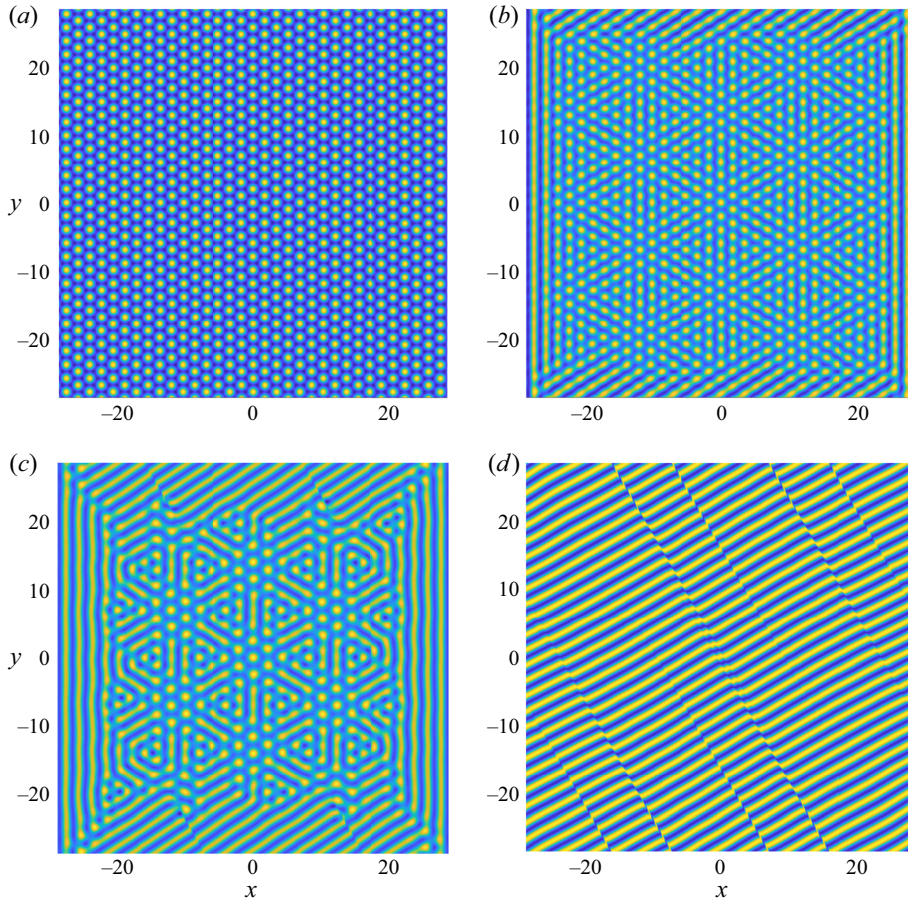


FIGURE 24. Initial condition (\mathcal{P}_2): hexagons with $q = 0.55$, $\epsilon = 0.3$, $r = 2.5$, $\alpha = 10^{-4}$ and $Pr = 50$. The reconstructed vertical velocity w is shown at different times: (a) $t = 0$, (b) $t = 2$, (c) $t = 10$ and (d) $t = 100$.

the final state consists of hexagons. We note that the transition from rolls to hexagons undergoes pearling, which gradually leads to separation into hexagons similarly as in Van-Den-Berg *et al.* (2015).

Remark. When there is no distortion of hexagons, i.e. when $\alpha_1 = \alpha_2 = 0$, in (4.22), the competition between uniform rolls and uniform hexagons is governed by the free energy density difference between them as indicated by Young & Riecke (2002), Sushchik & Tsimring (1994) and Hoyle (2006). For a given wavenumber $k = k_c + q$, hexagons have lower energy than rolls, and, therefore, are more stable at ϵ lower than a threshold value ϵ_f at which rolls and hexagons have the same free energy. Rolls are energetically favoured above ϵ_f . To determine ϵ_f , we compare the free energy density for perfect rolls,

$$F_r = -\frac{\epsilon - q^2 \xi_0^2}{\tau_0} R_0^2 + \frac{g_1}{2} R_0^4, \quad (8.1)$$

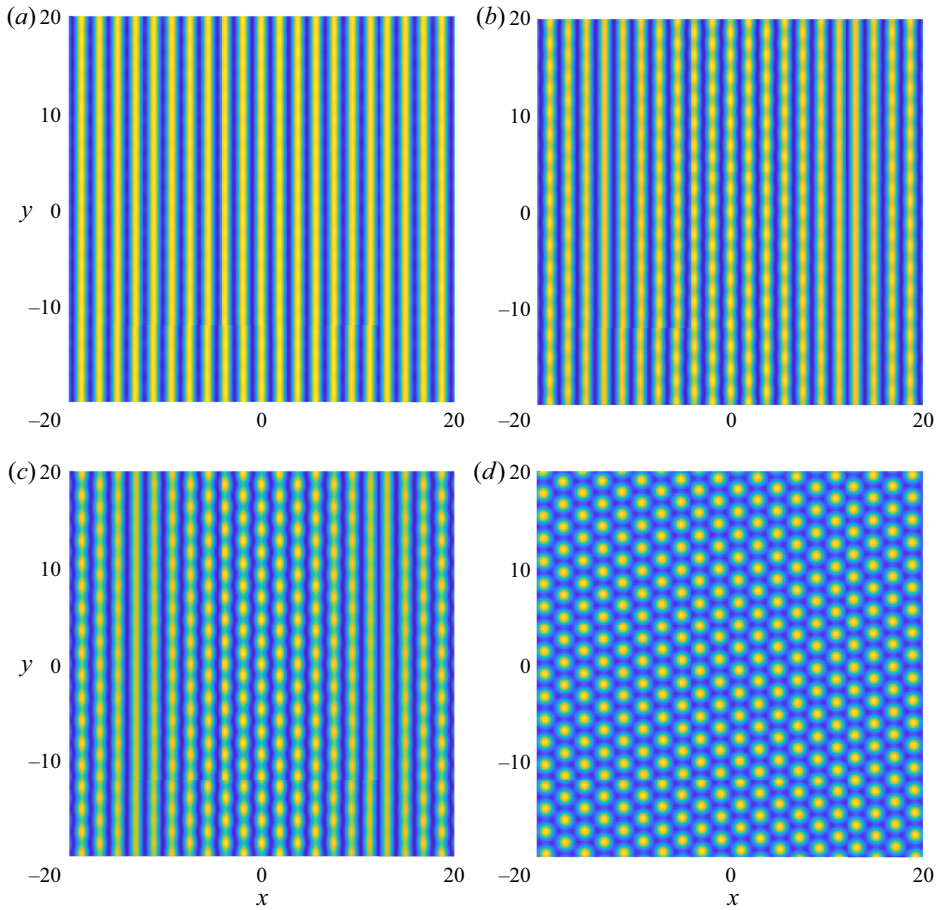


FIGURE 25. Initial condition (\mathcal{P}_3): rolls with $q = 0.25$, $\epsilon = 0.1$, $r = 2.5$, $\alpha = 10^{-4}$ and $Pr = 50$. The reconstructed vertical velocity w is shown at different times: (a) $t = 0$, (b) $t = 11$, (c) $t = 15$ and (d) $t = 2000$.

and for perfect hexagons,

$$F_h = -3 \frac{\epsilon - q^2 \xi_0^2}{\tau_0} H_0^2 - 2\zeta H_0^3 + \frac{3}{2} (g_1 + 2g_2) H_0^4. \quad (8.2)$$

It can be shown that $F_r = F_h$ at

$$\epsilon_f = \frac{\tau_0 \zeta^2 [g_1^2 + 3g_1 g_2 + \sqrt{2g_1} (g_1 + g_2)^{3/2}]}{2 (g_2 + 2g_2) (g_1 - g_2)^2} + q^2 \xi_0^2. \quad (8.3)$$

Figure 26 shows the variation of ϵ_f with the shear-thinning degree α for $q = 0.55$, $r = 2.5$ and $Pr = 50$. The nonlinearity of the rheological law favours rolls rather than hexagons. Values of ϵ_f are found higher (but in reasonable agreement) than the real threshold for hexagon–roll transition obtained from our numerical simulations. As explained by Sushchik & Tsimring (1994), the difference is due to the fact that the simple energetic analysis used in the determination of ϵ_f does not take into account the non-uniform structure of defects. Note that when $\alpha_1 = \alpha_2 = 0$, the final state consists of perfect rolls or perfect hexagons.

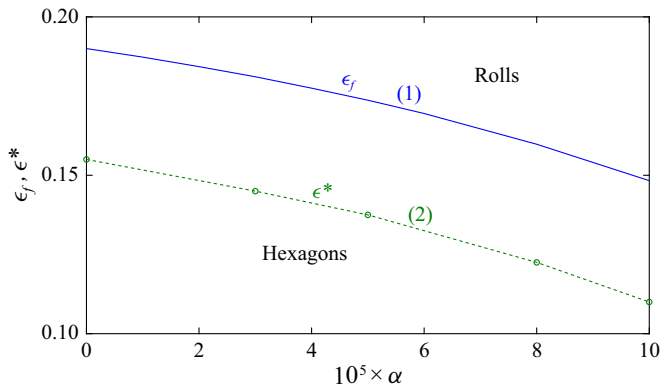


FIGURE 26. Threshold for hexagon–roll transition in the case where there is no distortion of hexagons as a function of the shear-thinning degree, with $q = 0.55$, $r = 2.5$ and $Pr = 50$. (1) Curve of equal energy for hexagons and rolls, (2) numerical simulations.

9. Conclusion

We have investigated the influence of shear-thinning effects on Rayleigh–Bénard convection for a Carreau fluid, taking into account the variation of the viscosity with temperature. The dependence of the viscosity on temperature was assumed of exponential type. A weakly nonlinear analysis using a multiple scale is adopted as a first approach to investigate the nonlinear effects. Generalized Ginzburg–Landau equations are obtained including spatial non-variational terms which account for the distortion of hexagons. The coefficients of these equations have been explicitly calculated and correlations are proposed. The steady solutions of these equations that correspond to rolls and hexagons have been obtained and their relative stability has been determined. Past the onset of convection, hexagonal cells with upward motion in the centre are selected in agreement with the experimental results of Darbouli *et al.* (2016) and Bouteraa (2016). The range of Rayleigh numbers associated with the subcritical convection is very narrow ($|\epsilon_h| \ll 1$) and difficult to detect experimentally. It is all the more reduced as shear-thinning effects are strong. For higher supercritical values, coexistence between hexagons and rolls is predicted in agreement with the experimental observations of Darbouli *et al.* (2016) and Bouteraa (2016). The range of Ra for which hexagons are stable increases with increasing viscosity ratio and decreases with increasing shear-thinning effects. This behaviour is along the same lines as the conclusion of Bouteraa *et al.* (2015), where it is shown that the nonlinearities introduced by the rheological law reinforce the stability of rolls. The stability of hexagons with respect to long wavelength perturbations is then addressed. Phase equations are derived and the band of stable wavenumbers is determined. Two types of long wavelength instabilities are identified: longitudinal and transverse phase instabilities. It is found that the stable hexagons domain is delimited mainly by the transverse phase instability. Furthermore, it is shown that the additional spatial nonlinear terms break the symmetry around k_c : the band of stable wavenumbers is open and decentred to the right, i.e. to wavenumbers larger than the critical one. This result is likewise in agreement with the experimental observations of M. Bouteraa (personal communication 2020), where the measured wavenumber increases with Ra . The theoretical calculations predict also that the band of stable wavenumbers becomes more decentred with increasing shear-thinning effects.

The numerical integration of the amplitude equations supports the theoretical results, enables us to illustrate the nonlinear evolution of the transverse phase instability and

highlights the role of the non-variational terms in the dynamics of pattern formation. At low ϵ , the transition from perfect hexagons, with a wavenumber outside the stable domain, to a new hexagonal pattern involves penta-hepta defects. Their number, large in the beginning of the process, decreases with time. For larger $\epsilon > \epsilon^*$, the transverse phase instability triggers the transition from regular hexagons to a disordered state of rolls with grain boundaries. The impact of the non-variational terms in the amplitude equations on the pattern dynamics is discussed. We have also performed a numerical simulation starting from a given initial pattern of rolls at $\epsilon < \epsilon_r$. The rolls-hexagons transition occurs through a progressive pearling leading to the creation of spots.

This study will be continued by considering larger values of the viscosity ratio r , for which we have a competition between squares and hexagons. In addition it would be useful to consider the temperature-dependence of other material properties such as the volumetric thermal expansion coefficient. There are other possible areas of future work. For instance, an investigation could be carried out to include side wall effects. Also, it would be interesting to analyse the influence of defects (pentagon-heptagon pair), which emerge in the hexagonal pattern, on the transition between different symmetries as well as on the wavenumber selection. Finally, we hope that the present work suggests new experiments to study the influence of shear-thinning effects on the selection of the convective pattern and its stability for high supercritical values of Ra , using experimental apparatus of larger aspect ratio comparatively to Darbouli *et al.* (2016) and Bouteraa (2016).

Appendix A. Operators and matrix coefficients

The coefficients of the matrices in (4.7)–(4.8) are given below:

A.1. The operator M

$$M = \begin{pmatrix} M_{11} & 0 & 0 & 0 \\ M_{21} & M_{22} & 0 & 0 \\ M_{31} & 0 & M_{33} & 0 \\ 0 & 0 & 0 & 1 \end{pmatrix}, \tag{A 1}$$

with

$$\left. \begin{aligned} M_{11} &= Pr^{-1} \Delta, & M_{21} &= \frac{\partial^2}{\partial x \partial z}, & M_{22} &= \nabla_{Hx}^2, \\ M_{31} &= \frac{\partial^2}{\partial y \partial z}, & M_{33} &= \nabla_{Hx}^2. \end{aligned} \right\} \tag{A 2}$$

A.1.1. The sub-scale $M^{(0)}$

The coefficients of $M^{(0)}$ in (4.7) are

$$\left. \begin{aligned} M_{11}^{(0)} &= Pr^{-1} \left(\Delta_{Hx} + \frac{\partial^2}{\partial z^2} \right), \\ M_{21}^{(0)} &= \frac{\partial^2}{\partial x \partial z}, & M_{22}^{(0)} &= \Delta_{Hx}, \\ M_{31}^{(0)} &= \frac{\partial^2}{\partial y \partial z}, & M_{33}^{(0)} &= \Delta_{Hx}, \\ M_{44}^{(0)} &= 1. \end{aligned} \right\} \tag{A 3}$$

A.1.2. The sub-scale $M^{(1)}$

The coefficients of $M^{(1)}$ in (4.7) are

$$\left. \begin{aligned} M_{11}^{(1)} &= 2Pr^{-1} \nabla_{Hx} \cdot \nabla_{HX}, \\ M_{21}^{(1)} &= \frac{\partial^2}{\partial X \partial z}, & M_{22}^{(1)} &= 2 \nabla_{Hx} \cdot \nabla_{HX}, \\ M_{31}^{(1)} &= \frac{\partial^2}{\partial Y \partial z}, & M_{33}^{(1)} &= 2 \nabla_{Hx} \cdot \nabla_{HX}, \\ M_{44}^{(1)} &= 0. \end{aligned} \right\} \tag{A 4}$$

A.2. The operator L

The coefficients of the 4×4 matrix L in (2.20) are given by

$$L = \begin{pmatrix} L_{11} & 0 & 0 & L_{14} \\ L_{21} & L_{22} & 0 & 0 \\ L_{31} & 0 & L_{33} & 0 \\ 1 & 0 & 0 & \Delta \end{pmatrix}, \tag{A 5}$$

with

$$\left. \begin{aligned} L_{11} &= \mu_b \Delta^2 + 2 \frac{d\mu_b}{dz} \Delta \frac{\partial}{\partial z} + \frac{d^2\mu_b}{dz^2} \left(\frac{\partial^2}{\partial z^2} - \Delta_H \right), & L_{14} &= Ra \Delta_H, \\ L_{21} &= \mu_b \Delta \frac{\partial^2}{\partial x \partial z} + \frac{d\mu_b}{dz} \frac{\partial}{\partial z} \left(\frac{\partial^2}{\partial x \partial z} \right), & L_{22} &= \mu_b \Delta \Delta_H + \frac{d\mu_b}{dz} \frac{\partial}{\partial z} \Delta_H, \\ L_{31} &= \mu_b \Delta \frac{\partial^2}{\partial y \partial z} + \frac{d\mu_b}{dz} \frac{\partial}{\partial z} \left(\frac{\partial^2}{\partial y \partial z} \right), & L_{33} &= \mu_b \Delta \Delta_H + \frac{d\mu_b}{dz} \frac{\partial}{\partial z} \Delta_H. \end{aligned} \right\} \tag{A 6}$$

A.3. Sub-scale $L^{(0)}$

The components of $L^{(0)}$ in (4.8) are

$$\left. \begin{aligned} L_{11}^{(0)} &= \mu_b \left(\nabla_{Hx}^2 + \frac{\partial^2}{\partial z^2} \right)^2 + 2 \frac{d\mu_b}{dz} \left(\nabla_{Hx}^2 + \frac{\partial^2}{\partial z^2} \right) \frac{\partial}{\partial z} + \frac{d^2\mu_b}{dz^2} \left(\frac{\partial^2}{\partial z^2} - \nabla_{Hx}^2 \right), \\ L_{14}^{(0)} &= Ra_c \nabla_{Hx}^2, \\ L_{21}^{(0)} &= \mu_b \left(\nabla_{Hx}^2 + \frac{\partial^2}{\partial z^2} \right) \frac{\partial^2}{\partial x \partial z} + \frac{d\mu_b}{dz} \frac{\partial}{\partial z} \left(\frac{\partial^2}{\partial x \partial z} \right), \\ L_{22}^{(0)} &= \mu_b \left(\nabla_{Hx}^2 + \frac{\partial^2}{\partial z^2} \right) \nabla_{Hx}^2 + \frac{d\mu_b}{dz} \frac{\partial}{\partial z} \nabla_{Hx}^2, \\ L_{31}^{(0)} &= \mu_b \left(\nabla_{Hx}^2 + \frac{\partial^2}{\partial z^2} \right) \frac{\partial^2}{\partial y \partial z} + \frac{d\mu_b}{dz} \frac{\partial}{\partial z} \left(\frac{\partial^2}{\partial y \partial z} \right), \\ L_{33}^{(0)} &= L_{22}^{(0)}, \\ L_{41}^{(0)} &= 1, & L_{44}^{(0)} &= \left(\nabla_{Hx}^2 + \frac{\partial^2}{\partial z^2} \right). \end{aligned} \right\} \tag{A 7}$$

A.4. Sub-scale $L^{(1)}$

The components of $L^{(1)}$ in (4.8) are

$$\left. \begin{aligned}
 L_{11}^{(1)} &= 4\mu_b \left(\nabla_{Hx}^2 + \frac{\partial^2}{\partial z^2} \right) (\nabla_{Hx} \cdot \nabla_{HX}) + 4 \frac{d\mu_b}{dz} (\nabla_{Hx} \cdot \nabla_{HX}) \frac{\partial}{\partial z} - 2 \frac{d^2\mu_b}{dz^2} (\nabla_{Hx} \cdot \nabla_{HX}), \\
 L_{14}^{(1)} &= Ra^{(1)} \nabla_{Hx}^2 + 2Ra_c (\nabla_{Hx} \cdot \nabla_{HX}), \\
 L_{21}^{(1)} &= \mu_b \left(\nabla_{Hx}^2 + \frac{\partial^2}{\partial z^2} \right) \frac{\partial^2}{\partial X \partial z} + 2\mu_b (\nabla_{Hx} \cdot \nabla_{HX}) \frac{\partial^2}{\partial x \partial z} + \frac{d\mu_b}{dz} \frac{\partial^2}{\partial z^2} \frac{\partial}{\partial X}, \\
 L_{22}^{(1)} &= 2\mu_b \left[\frac{\partial^2}{\partial z^2} + 2 \left(\frac{\partial^2}{\partial x^2} + \frac{\partial^2}{\partial y^2} \right) \right] (\nabla_{Hx} \cdot \nabla_{HX}) + 2 \frac{d\mu_b}{dz} (\nabla_{Hx} \cdot \nabla_{HX}) \frac{\partial}{\partial z}, \\
 L_{31}^{(1)} &= \mu_b \left[\nabla_{Hx}^2 \frac{\partial^2}{\partial Y \partial z} + 2 \nabla_{Hx} \cdot \nabla_{HX} + \frac{\partial^2}{\partial z^2} \frac{\partial^2}{\partial Y \partial z} \right] + \frac{d\mu_b}{dz} \frac{\partial^2}{\partial z^2} \frac{\partial}{\partial Y}, \\
 L_{41}^{(1)} &= 0, \quad L_{44}^{(1)} = 2 \nabla_{Hx} \cdot \nabla_{HX}.
 \end{aligned} \right\} \quad (A8)$$

A.5. Sub-scale $L^{(2)}$

The components of $L^{(2)}$ in (4.8) are

$$\left. \begin{aligned}
 L_{11}^{(2)} &= \mu_b \left[2 \left(\nabla_{Hx}^2 + \frac{\partial^2}{\partial z^2} \right) \nabla_{HX}^2 + 4 (\nabla_{Hx} \cdot \nabla_{HX})^2 \right] + 2 \frac{d\mu_b}{dz} \nabla_{HX}^2 \frac{\partial}{\partial z} - \frac{d^2\mu_b}{dz^2} \nabla_{HX}^2, \\
 L_{14}^{(2)} &= Ra_c \nabla_{HX}^2 + 2Ra^{(1)} (\nabla_{Hx} \cdot \nabla_{HX}) + Ra^{(2)} \nabla_{Hx}^2, \\
 L_{21}^{(2)} &= \mu_b \left[2 (\nabla_{Hx} \cdot \nabla_{HX}) \frac{\partial^2}{\partial X \partial z} + \nabla_{HX}^2 \frac{\partial^2}{\partial x \partial z} \right], \\
 L_{22}^{(2)} &= \mu_b \left(\frac{\partial^2}{\partial z^2} + \nabla_{Hx}^2 \right) \nabla_{HX}^2 + 4\mu_b (\nabla_{Hx} \cdot \nabla_{HX})^2 + \mu_b \nabla_{HX}^2 \nabla_{Hx}^2, \\
 L_{31}^{(2)} &= \mu_b \left[2 (\nabla_{Hx} \cdot \nabla_{HX}) \frac{\partial^2}{\partial Y \partial z} + \nabla_{HX}^2 \frac{\partial^2}{\partial y \partial z} \right], \\
 L_{41}^{(2)} &= 0, \quad L_{44}^{(2)} = \nabla_{HX}^2.
 \end{aligned} \right\} \quad (A9)$$

Appendix B. Second-order solution (hexagons)

B.1. Solution proportional to $|A_p|^2$ (zero mode)

The first component of the second-order solution, proportional to $|A_p|^2$, provides a correction of the basic state. Considering the w -equation, it is shown that the factor of $|A_1|^2$, $|A_2|^2$ and $|A_3|^2$ in the nonlinear inertial $NI_w^{(2)}$ and viscous $NV_w^{(2)}$ terms vanishes;

therefore,

$$w_1^{(2)} = 0. \tag{B 1}$$

Here $w_1^{(2)}$ means the first component of the second-order solution. Similarly, for the horizontal velocity, we have

$$u_1^{(2)} = v_1^{(2)} = 0. \tag{B 2}$$

There is no velocity for the zero mode. The correction of the conductive temperature profile can be written as $\theta_1^{(2)} = T_1(z)[|A_1|^2 + |A_2|^2 + |A_3|^2]$, where $T_1(z)$ satisfies

$$D^2T_1 = 2[G_{11}(DF_{11}) + F_{11}(DG_{11})], \tag{B 3}$$

with

$$T_1 = 0 \quad \text{at } z = 0 \text{ and } z = 1. \tag{B 4}$$

As for the linear problem, (B 3) with the boundary conditions (B 4) is solved numerically using a spectral Chebyshev collocation method.

B.2. Solution proportional to $A_p^2 \exp(2i\mathbf{k}_p \cdot \mathbf{r})$

The second component of the second-order solution, proportional to $A_p^2 E_p^2$, where $E_p = \exp(i\mathbf{k}_p \cdot \mathbf{r})$ represents the first harmonic of the fundamental. We have

$$(w_2^{(2)}, \theta_2^{(2)}) = (W_2(z), T_2(z)) (A_1^2 E_1^2 + A_2^2 E_2^2 + A_3^2 E_3^2) + \text{c.c.}, \tag{B 5}$$

with

$$\left[\mu_b (D^2 - 4k_c^2)^2 + 2 \frac{d\mu_b}{dz} (D^3 - 4k_c^2 D) + \frac{d^2\mu_b}{dz^2} (D^2 + 4k_c^2) \right] W_2 - 4k_c^2 Ra_c T_2 = \frac{2}{Pr} (F_{11} D^3 F_{11} - DF_{11} D^2 F_{11}) - [NV_w]_{A_p^2 E_p^2}^{(2)}, \tag{B 6}$$

$$W_2 + (D^2 - 4k_c^2) T_2 = F_{11} DG_{11} - G_{11} DF_{11}. \tag{B 7}$$

The boundary conditions on W_2 and T_2 are identical to those on F_{11} and G_{11} , (3.4).

Concerning the horizontal velocity, we have

$$\nabla_{Hx}^2 \mathbf{u}_{H2}^{(2)} + \nabla_{Hx} \frac{\partial w_2^{(2)}}{\partial z} = 0. \tag{B 8}$$

We obtain

$$\mathbf{u}_{H2}^{(2)} = \frac{DW_2}{4k_c^2} \nabla_{Hx} [A_1^2 E_1^2 + A_2^2 E_2^2 + A_3^2 E_3^2] + \text{c.c.} \tag{B 9}$$

B.3. Solution proportional to $A_p A_q^* E_p E_q^*$

The third component of the second-order solution, proportional to $A_p A_q^* E_p E_q^*$, reads as

$$(w_3^{(2)}, \theta_3^{(2)}) = (W_3(z), T_3(z)) (A_1 A_2^* E_1 E_2^* + A_1 A_3^* E_1 E_3^* + A_2 A_3^* E_2 E_3^*) + \text{c.c.}, \tag{B 10}$$

with

$$\begin{aligned} & \left[\mu_b (D^2 - 3k_c^2)^2 + 2 \frac{d\mu_b}{dz} (D^3 - 3k_c^2 D) + \frac{d^2 \mu_b}{dz^2} (D^2 + 3k_c^2) \right] W_3 - 3k_c^2 Ra_c T_3 \\ & = \frac{3}{Pr} (F_{11} D^3 F_{11} - k_c^2 F_{11} D F_{11}) - [NV_w]_{E_p E_q^*}^{(2)}, \end{aligned} \tag{B 11}$$

$$W_3 + (D^2 - 3k_c^2) T_3 = 2F_{11} D G_{11} - G_{11} D F_{11}. \tag{B 12}$$

Boundary conditions on (W_3, T_3) are the same as the ones on (F_{11}, G_{11}) .

The horizontal velocity components satisfy

$$\nabla_{Hx}^2 \mathbf{u}_{H3}^{(2)} + \nabla_{Hx} \frac{\partial w_3^{(2)}}{\partial z} = 0. \tag{B 13}$$

We obtain

$$\mathbf{u}_{H3}^{(2)} = \frac{D W_3}{3k_c^2} \nabla_{Hx} (A_1 A_2^* E_1 E_2^* + A_1 A_3^* E_1 E_3^* + A_2 A_3^* E_2 E_3^*) + \text{c.c.} \tag{B 14}$$

B.4. Solution proportional to $\exp(i\mathbf{k}_p \cdot \mathbf{r})$

The fourth component of the second-order solution is proportional to $\exp(i\mathbf{k}_p \cdot \mathbf{r})$ (resonant term). The solution is achieved using the solvability condition. It is shown that it can be written as

$$(w_4^{(2)}, \theta_4^{(2)}) = (W_{41}, T_{41}) E_1 + (W_{42}, T_{42}) E_2 + (W_{43}, T_{43}) E_3 + \text{c.c.}, \tag{B 15}$$

with

$$\begin{aligned} & \left[\mu_b \left(\frac{\partial^2}{\partial z^2} - k_c^2 \right)^2 + 2 \frac{d\mu_b}{dz} \left(\frac{\partial^2}{\partial z^2} - k_c^2 \right) \frac{\partial}{\partial z} + \frac{d^2 \mu_b}{dz^2} \left(\frac{\partial^2}{\partial z^2} + k_c^2 \right) \right] W_{41} - Ra_c k_c^2 T_{41} \\ & = \left[-4i\mu_b (D^2 - k_c^2) F_{11} - 4i \frac{d\mu_b}{dz} D F_{11} + 2i \frac{d^2 \mu_b}{dz^2} F_{11} \right] (\mathbf{k}_1 \cdot \nabla_{HX}) A_1 \\ & \quad + k_c^2 Ra_1 G_{11} A_1 - 2i Ra_c G_{11} (\mathbf{k}_2 \cdot \nabla_{HX}) A_1 \\ & \quad + \frac{1}{Pr} (F_{11} D^3 F_{11} + 2D F_{11} D^2 F_{11} - 3k_c^2 F_{11} D F_{11}) A_2^* A_3^* - [NV_w]_{E_1}^{(2)} A_2^* A_3^*, \end{aligned} \tag{B 16}$$

$$W_{41} + (D^2 - k_c^2) T_{41} = -2i G_{11} (\mathbf{k}_1 \cdot \nabla_{HX}) A_1 + (2F_{11} D G_{11} + G_{11} D F_{11}) A_2^* A_3^*. \tag{B 17}$$

Two others similar systems of equations are obtained for (W_{42}, T_{42}) and (W_{43}, T_{43}) by the circular permutation of indices. Note that according to (4.18), $Ra^{(1)} A_1$ can be written in

terms of $A_2^* A_3^*$. The system of differential equations (B 16), (B 17) can be written formally as $[A](W_{41}, T_{41})^t = [X]A_2^* A_3^* + Z(2i)(\mathbf{k}_1 \cdot \nabla_{HX})A_1$.

Hence, $(W_{41}, T_{41})^t = (W_s, T_s)^t A_2^* A_3^* + (\tilde{W}_s, \tilde{T}_s)^t 2i(\mathbf{k}_1 \cdot \nabla_{HX})A_1$, where $(W_s, T_s)^t = [A]^{-1}[X]$ and $(\tilde{W}_s, \tilde{T}_s)^t = [A]^{-1}[Z]$. The boundary conditions on W_s and T_s are the same as the ones on (F_{11}, G_{11}) .

For the horizontal velocity, we have

$$\mathbf{u}_{H4}^{(2)} = U_{H41}E_1 + U_{H42}E_2 + U_{H43}E_3 + \text{c.c.}, \tag{B 18}$$

with

$$\begin{aligned} &\mu_b \left(\frac{\partial^2}{\partial z^2} - k_c^2 \right) \left(-k_c^2 U_{H41} + i\mathbf{k}_1 \frac{\partial W_{41}}{\partial z} \right) \\ &+ \frac{d\mu_b}{dz} \left(-k_c^2 \frac{\partial}{\partial z} U_{H41} + i\mathbf{k}_1 \frac{\partial^2 W_{41}}{\partial z^2} \right) = 2 \frac{d\mu_b}{dz} D^2 F_{11} \nabla_{HX} A_1 \\ &+ \left[\mu_b (D^3 F_{11} - k_c^2 D F_{11}) + \frac{d\mu_b}{dz} D^2 F_{11} \right] \left[2 \frac{\mathbf{k}_1}{k_c^2} (\mathbf{k}_1 \cdot \nabla_{HX}) A_1 - \nabla_{HX} A_1 \right]. \end{aligned} \tag{B 19}$$

Two other similar equations are obtained for U_{H42} and U_{H43} .

Appendix C. Adjoint eigenvalue problem: adjoint mode

In the analysis developed in § 4, it is necessary to eliminate secular terms in non-homogeneous differential equations, i.e. the solvability condition must be applied. It is therefore necessary to determine the linear adjoint of the direct problem at the critical conditions. For vector fields \mathbf{f} and \mathbf{g} , one defines an inner product between two vector functions $\mathbf{f}(z)$ and $\mathbf{g}(z)$ by

$$\langle \mathbf{f}, \mathbf{g} \rangle = \int_0^1 \mathbf{f}^* \cdot \mathbf{g} \, dz, \tag{C 1}$$

where \mathbf{f}^* is the complex conjugate of \mathbf{f} . To the direct eigenvalue problem (3.5) corresponds the adjoint problem

$$s\tilde{M}^+ \cdot X_{ad} = \tilde{L}^+ \cdot X_{ad} \quad \text{with } X_{ad} = (F_{ad}, G_{ad}), \tag{C 2}$$

where the adjoint operators \tilde{M}^+ and \tilde{L}^+ are defined by

$$\langle X_{ad}, \tilde{M} \cdot X_{11} \rangle = \langle \tilde{M}^+ \cdot X_{ad}, X_{11} \rangle, \quad \langle X_{ad}, \tilde{L} \cdot X_{11} \rangle = \langle \tilde{L}^+ \cdot X_{ad}, X_{11} \rangle, \tag{C 3a,b}$$

where X_{11} fulfils the ‘linear’ boundary conditions (3.4). By integrating by parts we get the linear adjoint problem and the corresponding boundary conditions

$$\begin{aligned} sPr^{-1} (D^2 - k^2) F_{ad} &= \mu_b (D^2 - k^2)^2 F_{ad} + 2D\mu_b (D^2 - k^2) D F_{ad} \\ &+ D^2 \mu_b (D^2 + k^2) F_{ad} + G_{ad}, \end{aligned} \tag{C 4}$$

$$sG_{ad} = -k^2 Ra F_{ad} + (D^2 - k^2) G_{ad}, \tag{C 5}$$

with

$$F_{ad} = 0, \quad DF_{ad} = 0, \quad G_{ad} = 0 \quad \text{at } z = 0, \tag{C 6a}$$

$$F_{ad} = 0, \quad DF_{ad} = 0, \quad G_{ad} = 0 \quad \text{at } z = 1. \tag{C 6b}$$

The solution of these equations is obtained using the same method as for the direct eigenvalue problem. Similarly, the normalization adopted for the adjoint mode is

$$G_{ad}(z = 1/2) = 1. \tag{C 7}$$

At $Ra = Ra_c$, the so-called adjoint critical mode does not depend on the Prandtl number.

Appendix D. Cubic-order solution

At order δ^3 , we have

$$\begin{aligned} L_{11}^{(0)}w^{(3)} + L_{14}^{(0)}\theta^{(3)} &= M_{11}^{(0)}\frac{\partial}{\partial T}w^{(1)} - L_{11}^{(1)}w^{(2)} - L_{14}^{(1)}\theta^{(2)} \\ &\quad - L_{11}^{(2)}w^{(1)} - L_{14}^{(2)}\theta^{(1)} - NI_w^{(3)} - NV_w^{(3)}, \end{aligned} \tag{D 1}$$

$$w^{(3)} + L_{44}^{(0)}\theta^{(3)} = \frac{\partial}{\partial T}\theta^{(1)} - L_{44}^{(1)}\theta^{(2)} - L_{44}^{(2)}\theta^{(1)} - NI_\theta^{(3)}. \tag{D 2}$$

D.1. Solution proportional to $\exp(i\mathbf{k}_p \cdot \mathbf{r})$

One component of the cubic-order solution $(w_1^{(3)}, \theta_1^{(3)})$ is proportional to $\exp(i\mathbf{k}_p \cdot \mathbf{r})$:

$$(w_1^{(3)}, \theta_1^{(3)}) = (W_{11}^{(3)}, T_{11}^{(3)})E_1 + (W_{12}^{(3)}, T_{12}^{(3)})E_2 + (W_{13}^{(3)}, T_{13}^{(3)})E_3 + \text{c.c.} \tag{D 3}$$

Projecting (D 1) and (D 2) onto the mode E_1 , for instance, gives formally

$$\begin{aligned} \mathcal{L}_{11}^{(0)}W_{11}^{(3)} + \mathcal{L}_{14}^{(0)}T_{11}^{(3)} &= \mathcal{M}_{11}^{(0)}F_{11}\frac{\partial A_1}{\partial T} - \mathcal{L}_{11}^{(1)}W_{41}^{(2)} - \mathcal{L}_{14}^{(1)}T_{41}^{(2)} \\ &\quad - \mathcal{L}_{11}^{(2)}F_{11}A_1 - \mathcal{L}_{14}^{(2)}G_{11}A_1 - [NI_w^{(3)}]_{E_1} - [NV_w^{(3)}]_{E_1}, \end{aligned} \tag{D 4}$$

$$W_{11}^{(3)} + \mathcal{L}_{44}^{(0)}T_{11}^{(3)} = G_{11}\frac{\partial A_1}{\partial T} - \mathcal{L}_{44}^{(1)}T_{41}^{(2)} - \mathcal{L}_{44}^{(2)}G_{11}A_1 - [NI_\theta^{(3)}]_{E_1}. \tag{D 5}$$

Note that $Ra^{(2)}$ appears in the operator $\mathcal{L}_{14}^{(2)}$:

$$\mathcal{L}_{14}^{(2)} = Ra_c \nabla_{HX}^2 + 2iRa^{(1)}(k_1 \cdot \nabla_{HX}) - k_c^2 Ra^{(2)}. \tag{D 6}$$

D.2. Determination of $Ra^{(2)}$

The system of (D 4)–(D 5) have a solution if and only if the right-hand side of (D 4)–(D 5) is orthogonal to the kernel of the adjoint operator (Fredholm alternative theorem).

Applying this theorem leads to an equation for $Ra^{(2)}$, which can be written formally as

$$\begin{aligned} Ra^{(2)}A_1 &= I_1 \frac{\partial A_1}{\partial T} + I_2 (\mathbf{k}_1 \cdot \nabla_{HX})^2 A_1 \\ &+ I_3 |A_1|^2 A_1 + I_4 |A_2|^2 A_1 + I_5 |A_3|^2 A_1 \\ &+ I_6 A_2^* \frac{\partial A_3^*}{\partial X} + I_6 A_3^* \frac{\partial A_2^*}{\partial X} + I_7 A_2^* \frac{\partial A_3^*}{\partial Y} + I_8 A_3^* \frac{\partial A_2^*}{\partial Y}, \end{aligned} \quad (D 7)$$

where

$$I_1 = \int_0^1 \left[\frac{1}{Pr} (D^2 - k_c^2) F_{11} F_{ad} + G_{11} G_{ad} \right] dz \quad (D 8)$$

is the coefficient proportional to $\partial A_1 / \partial T$, and similarly for I_2, I_3, \dots

Appendix E. Correlations proposed by Busse for a Newtonian fluid

Assuming a linear variation of the viscosity with temperature, the following correlations for ϵ_a, ϵ_r and ϵ_h are proposed by Busse (1967). The revised version of these correlations given by Bodenschatz *et al.* (2000) is used here. They are represented by dashed lines in figure 16.

$$\epsilon_a = -\mathcal{P}^2 / (4R_h Ra_c), \quad (E 1)$$

$$\epsilon_r = 3\mathcal{P}^2 R_r / (L^2 Ra_c), \quad (E 2)$$

$$\epsilon_h = (9R_h - 3L)\mathcal{P}^2 / (L^2 Ra_c), \quad (E 3)$$

with

$$\mathcal{P} = \gamma_2 \mathcal{P}_2; \quad \gamma_2 = 2(1-r)/(1+r); \quad \mathcal{P}_2 = 2.755, \quad (E 4)$$

$$R_h = 0.89360 + 0.04959/Pr + 0.06787/Pr^2, \quad (E 5)$$

$$R_r = 0.69942 - 0.00472/Pr + 0.00832/Pr^2, \quad (E 6)$$

$$L = 0.29127 + 0.08147/Pr + 0.08933/Pr^2. \quad (E 7)$$

REFERENCES

- ALBAALBAKI, B. & KHAYAT, R. 2011 Pattern selection in the thermal convection of non-Newtonian fluids. *J. Fluid Mech.* **668**, 500–550.
- ALLOUI, Z., BEN-KHELIFA, N., BEJI, H., VASSEUR, P. & GUIZANI, A. 2013 The onset of convection of power-law fluids in a shallow cavity heated from below by a constant heat flux. *J. Non-Newtonian Fluid Mech.* **196**, 70–82.
- BALMFORTH, N. J. & RUST, A. C. 2009 Weakly nonlinear viscoplastic convection. *J. Non-Newtonian Fluid Mech.* **158**, 36–45.
- BENOUARED, O., MAMOU, M. & AIT-MESSAOUDENE, N. 2014 Numerical nonlinear analysis of subcritical Rayleigh–Bénard convection in a horizontal confined enclosure filled with non-Newtonian fluids. *Phys. Fluids* **26** (7), 073101.
- BIRD, R. B., AMSTRONG, R. & HASSAGER, O. 1987 *Dynamics of Polymeric Liquids*. Wiley-Interscience.
- BODENSCHATZ, E., PESCH, W. & AHLERS, G. 2000 Recent developments in Rayleigh–Bénard convection. *Annu. Rev. Fluid Mech.* **32**, 709–778.

- BOTTARO, A., METZENER, P. & MATALON, M. 1992 Onset and two-dimensional patterns of convection with strongly temperature-dependent viscosity. *Phys. Fluids* **4** (4), 655–663.
- BOUTERAA, M. 2016 Convection de Rayleigh–Bénard pour des fluides rhéofluidifiants: approche théorique et expérimentale. PhD thesis, Université de Lorraine.
- BOUTERAA, M., NOUAR, C., PLAUT, E., MÉTIVIER, C. & KALCK, A. 2015 Weakly nonlinear analysis of Rayleigh–Bénard convection in shear-thinning fluids: nature of the bifurcation and pattern selection. *J. Fluid Mech.* **767**, 696–734.
- BRAGARD, J. & VELARDE, M. G. 1998 Bénard–Marangoni convection: planforms and related theoretical predictions. *J. Fluid Mech.* **368**, 165–194.
- BRAND, H. R. 1989 Envelope equations near the onset of a hexagonal pattern. *Prog. Theor. Phys. Suppl.* **99**, 442–449.
- BUSSE, F. H. 1967 The stability of finite amplitude cellular convection and its relation to an extremum principle. *J. Fluid Mech.* **30**, 625–649.
- BUSSE, F. H. 1978 Nonlinear properties of thermal convection. *Rep. Prog. Phys.* **41**, 1930–1967.
- BUSSE, F. H. & FRICK, H. 1985 Square-pattern convection in fluids with strongly temperature-dependent viscosity. *J. Fluid Mech.* **150**, 451–465.
- BUSSE, F. H. & WHITEHEAD, J. A. 1971 Instabilities of convection rolls in a high Prandtl number fluid. *J. Fluid Mech.* **47** (2), 305–320.
- CHARLSON, G. S. & SANI, R. L. 1970 Thermoconvective instability in a bounded cylindrical fluid layer. *Intl J. Heat Mass Transfer* **13** (9), 1479–1496.
- CILIBERTO, S., COULLET, P., LEGA, J., PAMPALONI, E. & PEREZ-GARCIA, C. 1990 Defects in roll-hexagon competition. *Phys. Rev. Lett.* **65** (19), 2370.
- CILIBERTO, S., PAMPALONI, E. & PEREZ-GARCIA, C. 1988 Competition between different symmetries in convective patterns. *Phys. Rev. Lett.* **61** (10), 1198.
- CLEVER, R. M. & BUSSE, F. H. 1974 Transition to time-dependent convection. *J. Fluid Mech.* **65** (4), 625–645.
- COX, S. M. & MATTHEWS, P. C. 2002 Exponential time differencing for stiff systems. *J. Comput. Phys.* **176** (2), 430–455.
- DARBOULI, A., MÉTIVIER, C., LECLERC, S., NOUAR, C. & STEMMLER, D. 2016 Natural convection in shear-thinning fluids: experimental investigation by MRI. *Intl J. Heat Mass Transfer* **95**, 742–754.
- DAVILLE, A. & JAUPART, P. 1993 Transient high Rayleigh number thermal convection with large viscosity variation. *J. Fluid Mech.* **253**, 141–166.
- ECHEBARRIA, B. & PEREZ-GARCIA, C. 2001 Stability of hexagonal pattern in Bénard–Marangoni convection. *Phys. Rev. E* **63**, 066307.
- ECHEBARRÍA, B. & PÉREZ-GARCÍA, C. 1998 Phase instabilities in hexagonal patterns. *Europhys. Lett.* **43** (1), 35.
- GETLING, A. V. 1988 *Rayleigh–Bénard Convection: Structures and Dynamics*. World Scientific.
- GOLUBITSKY, M., SWIFT, J. W. & KNOBLOCK, E. 1984 Symmetries and pattern selection in Rayleigh–Bénard convection. *Physica D* **10**, 249–276.
- HOARD, C. Q., ROBERTSON, C. R. & ACRIVOS, A. 1970 Experiments on the cellular structure in Bénard convection. *Intl J. Heat Mass Transfer* **13**, 849–856.
- HOYLE, R. 1995 Nonlinear phase diffusion equations for the long-wave instabilities of hexagons. *Appl. Maths Lett.* **8**, 81–85.
- HOYLE, R. 2006 *Pattern Formation: An Introduction Methods*. Cambridge University Press.
- JENKINS, D. R. 1987 Rolls versus squares in thermal convection of fluids with temperature-dependent viscosity. *J. Fluid Mech.* **178**, 491–506.
- JENNY, M., PLAUT, E. & BRIARD, A. 2015 Numerical study of subcritical Rayleigh–Bénard convection rolls in strongly shear-thinning Carreau fluids. *J. Non-Newtonian Fluid Mech.* **219**, 19–34.
- KADDIRI, M., NAÏMI, M., RAJI, A. & HASNAOUI, M. 2012 Rayleigh–Bénard convection of non-Newtonian power-law fluids with temperature-dependent viscosity. *ISRN Thermodyn.* **2012**. ID614712, 1–10.
- KOLODNER, P. 1998 Oscillatory convection in viscoelastic DNA suspensions. *J. Non-Newtonian Fluid Mech.* **75**, 167–192.

- LAMSAADI, M., NAIMI, M. & HASNAOUI, M. 2005 Natural convection of power law fluids in a shallow horizontal rectangular cavity uniformly heated from below. *Heat Mass Transfer* **41**, 239–249.
- LARSON, R. G. 1992 Instabilities in viscoelastic flows. *Rheol. Acta* **31** (3), 213–263.
- LAUZERAL, J., METENS, S. & WALGRAEF, D. 1993 On the phase dynamics of hexagonal patterns. *Europhys. Lett.* **24** (9), 707.
- LI, Z. & KHAYAT, R. E. 2005 Finite-amplitude Rayleigh–Bénard convection and pattern selection for viscoelastic fluids. *J. Fluid Mech.* **529**, 221–251.
- LIANG, S. F. & ACRIVOS, A. 1970 Experiments on buoyancy-driven convection in non-Newtonian fluids. *Rheol. Acta* **9**, 447–455.
- MCKENZIE, D. 1988 The symmetry of convective transitions in space and time. *J. Fluid Mech.* **191**, 287–339.
- PALM, E. 1960 On the tendency towards hexagonal cells in steady convection. *J. Fluid Mech.* **8**, 183–192.
- PALM, E. 1975 Nonlinear thermal convection. *Annu. Rev. Fluid Mech.* **7** (1), 39–61.
- PALM, E., ELLINGSEN, T. & GJEVIK, B. 1967 On the occurrence of cellular motion in Bénard convection. *J. Fluid Mech.* **30**, 651–661.
- PAMPALONI, E., PEREZ-GARCIA, C., ALBAVETTI, L. & CILIBERTO, S. 1992 Transition from hexagons to rolls in convection in fluids under non-Boussinesq conditions. *J. Fluid Mech.* **234**, 393–416.
- PENA, B. & PEREZ-GARCIA, C. 2001 Stability of Turing patterns in the Brusselator model. *Phys. Rev. E* **64** (5), 056213.
- POCHEAU, A. & CROQUETTE, V. 1984 Dislocation motion: a wavenumber selection mechanism in Rayleigh–Bénard convection. *J. Phys.* **45** (1), 35–48.
- RICHTER, F. M. 1978 Experiments on the stability of convection rolls in fluids whose viscosity depends on temperature. *J. Fluid Mech.* **89** (3), 553–560.
- SEGEL, L. A. & STUART, J. T. 1962 On the question of the preferred mode in cellular thermal convection. *J. Fluid Mech.* **13** (2), 289–306.
- SOLOMATOV, V. S. 1995 Scaling of temperature-and-stress-dependent viscosity convection. *Phys. Fluids* **7**, 266–274.
- SOLOMATOV, V. S. & BARR, A. C. 2006 Onset of convection in fluids with strongly temperature-dependent power-law viscosity. *Phys. Earth Planet. Inter.* **155** (1–2), 140–145.
- SOLOMATOV, V. S. & BARR, A. C. 2007 Onset of convection in fluids with strongly temperature-dependent, power-law viscosity: 2. Dependence on the initial perturbation. *Phys. Earth Planet. Inter.* **165** (1–2), 1–13.
- SOMERSCALES, E. F. C. & DOUGHERTY, T. S. 1970 Observed flow patterns at the initiation of convection in a horizontal liquid layer heated from below. *J. Fluid Mech.* **42** (4), 755–768.
- STENGEL, K. C., OLIVIER, D. S. & BOOKER, J. R. 1982 Onset of convection in a variable-viscosity fluid. *J. Fluid Mech.* **120**, 411–431.
- SUSHCHIK, M. M. & TSIMRING, L. S. 1994 The Eckhaus instability in hexagonal patterns. *Physica D* **74**, 90–106.
- TANNER, R. 2000 *Engineering Rheology*. Oxford University Press.
- VAN-DEN-BERG, J. B., DESCHÊNES, A., LESSARD, J. P. & MIRELES-JAMES, J. D. 2015 Stationary coexistence of hexagons and rolls via rigorous computations. *SIAM J. Appl. Dyn. Syst.* **14** (2), 942–979.
- WHITE, D. B. 1988 The planforms and the onset of convection with a temperature dependent-viscosity. *J. Fluid Mech.* **191**, 2247–286.
- YOUNG, Y. N. & RIECKE, H. 2002 Mean flow in hexagonal convection: stability and nonlinear dynamics. *Physica D* **163** (3–4), 166–183.